Journal of Materials Chemistry C

ROYAL SOCIETY OF CHEMISTRY

PAPER

View Article Online
View Journal | View Issue

Cite this: J. Mater. Chem. C, 2025, 13, 21179

Water-assisted proton conductivity and a magnetic study of heterotrinuclear oxalate-bridged compounds: molecular precursors for the Mn_2CrO_4 spinel

Ana Lozančić, [a] Sanja Burazer, [a] Tobias Wagner,[b] Krešimir Molčanov, [a] Damir Pajić, [c] Lidija Androš Dubraja, [a] Michael Tiemann [b] and Marijana Jurić *[a]

Novel oxalate-bridged heterotrinuclear complexes $[A][Mn_2Cr(bpy)_2(H_2O)_2Cl_2(C_2O_4)_3]$ (A = $(CH_3)_2(C_2H_5)NH^+$ (**1**) and $(CH_3)(C_2H_5)_2NH^+$ (**2**); bpy = 2,2′-bipyridine) were synthesized using an aqueous solution of $[A]_3[Cr(C_2O_4)_3]$ as a building block in reaction with Mn^{2+} ions and with the addition of the N-donor ligand bipyridine. The isostructural heterometallic complex salts were characterized by single-crystal and powder X-ray diffraction, infrared and impedance spectroscopy, thermal analysis and magnetization measurements. The trinuclear anion $[\{Mn(bpy)(H_2O)Cl(\mu\text{-}C_2O_4)\}_2Cr(C_2O_4)]^-$ consists of two $[Mn(bpy)(H_2O)Cl]^+$ units bridged by the $[Cr(C_2O_4)_3]^{3-}$ anion, which acts as a bidentate ligand towards each of the manganese atoms. The anions are hydrogen bonded to each other *via* coordinated chloride anions, water molecules and oxygen oxalate atoms, resulting in two-dimensional (2D) hydrogen bonding layers. Compounds exhibit water-assisted proton conductivity behaviour, which was investigated at different temperatures and relative humidities (RH). At 25 °C, an increase in RH from 60% to 93% resulted in an obvious proton conducting switch from 9.1×10^{-11} to 5.6×10^{-5} S cm^{-1} for **1** and from 7.4×10^{-10} to 1.8×10^{-6} S cm^{-1} for **2**, corresponding to high on/off ratios of about 10^6 for **1** and 10^4 for **2**. *In situ* powder X-ray diffraction (PXRD) analysis showed that unit cell parameters of compounds **1** and **2** slightly increase when exposed to humid conditions. This confirmed that incorporation of water molecules into structures with pores and voids causes the proton conductivity switching phenomenon. Magnetic susceptibility measurements indicate a ferromagnetic interaction between Cr^{3+} and Mn^{2+} ions bridged by the bis(bidentate) oxalate group. The prepared compounds **1** and **2** were explored as single-source precursors for the formation of spinel oxide by their thermal treatment. With increasing temperature, the spinel composition changed according to the formula $Mn_{1+x}Cr_{2-x}O_4$ ($0 \leq x \leq 1$), where x = 0.7 at 500 °C and x = 1 at 900 °C when $^{tet}[Mn^{II}]^{oct}[Mn^{III}Cr^{III}]O_4$ is formed. The (micro)structure, morphology, and optical properties of spinel Mn_2CrO_4 were characterized by PXRD, scanning electron microscopy and UV-Vis diffuse reflectance spectroscopy. The photocatalytic activity of this oxide in degradation of the methylene blue dye under Vis irradiation without and with the support of hydrogen peroxide was further investigated.

Received 4th July 2025,
Accepted 3rd September 2025

DOI: 10.1039/d5tc02569a

rsc.li/materials-c

Introduction

The development of proton-conductive materials in the solid state has attracted considerable attention in materials science and represents one of the greatest challenges, as they are used as solid-state electrolytes in a variety of applications, for example, in fuel cells and separation membranes. The study of stimuli-responsive materials has also attracted great interest in the interdisciplinary fields of materials science and chemistry in recent decades. This interest stems from the fact that all living organisms and soft materials are naturally able to respond and adapt to external stimuli. Due to their ability to adapt to various stimuli such as an electric field, solvents, light, heat and stress, these so-called ''smart materials'' are finding new applications in a variety of industries, including biomedicine, biotechnology, renewable energy, data storage, imaging and sensing, textiles, and smart coatings. The importance of

[a] Ruđer Bošković Institute, Bijenička cesta 54, 10000 Zagreb, Croatia. E-mail: Marijana.Juric@irb.hr
[b] Department of Chemistry, Faculty of Science, Paderborn University, Warburger Str. 100, 33098 Paderborn, Germany
[c] Department of Physics, Faculty of Science, University of Zagreb, Bijenička cesta 32, 10000 Zagreb, Croatia

proton transfer in living systems, in which electrical signals are transmitted and processed by protonic currents, has sparked interest in stimulus-induced proton (H^+) transport. In addition to practical applications such as drug delivery, sensors, memory, and display devices, the creation of artificial stimuli-responsive proton conductors is of interest for a deeper understanding of proton transport pathways.[1–4]

Recently, attention has been drawn to metal–organic coordination polymers as an emerging class of proton conducting materials due to their low cost, ability to function at moderate temperatures, highly customizable structures, high porosity and controllable surface areas.[5–8] In addition, proton-conducting coordination compounds with dielectric switching behaviour in response to external stimuli including electric fields, guest molecules, and light have gained increasing attention in recent years due to their potential applications in sensors, memory devices, and display technologies. In particular, studies focusing on humidity-induced switching of proton conductance have identified water molecules as suitable triggers because of their solid donor–acceptor capabilities and ease of control.[1,9–13]

It has been pointed out that the presence of a good proton carrier and a hydrogen-bonded arrangement in a proton conductor plays a crucial role. The number of protonated proton carriers acting as proton donors, the number of non-protonated sites acting as proton acceptors, and the effectiveness of the proton transport pathway consisting of the hydrogen-bonding network are the three conditions that must be met to obtain good conductivity in coordination compounds.[14–21] In general, there are three main approaches for the construction of proton conducting crystalline materials: (i) introduction of charged proton carriers as counterions (NH_4^+ and H_3O^+) during the synthesis to maintain the neutrality of the framework; (ii) incorporation of the acidic group such as non-coordinated functional groups in organic ligands (*e.g.*, $-OH$, $-COOH$, $-CONH_2$, $-SO_3H$, and $-PO_3H_2$) or coordination of protonated molecules at the metal centers; and (iii) embedding charge-neutral proton carriers (imidazole, triazole, and histamine) as guests in the pores.[9–13] In addition to two- (2D) and three-dimensional (3D) assemblies,[12–17] low-dimensional structures can also exhibit excellent proton conductivity properties *via* hydrogen-bonding networks, as a small void space can be advantageous for proton hopping.[18,19,21–26]

The oxalate anion, $C_2O_4^{2-}$, plays a key role in the development and production of multifunctional materials due to its diverse coordination possibilities to metal centers and its ability to mediate in the electrical effects between paramagnetic metal ions and successfully forms hydrogen-bonding networks. Using the "building block chemistry" approach, many (hetero)polynuclear species, namely, 2D and 3D anionic networks of the general formula $[M_a^{II/III}M_b^{I/II}(C_2O_4)]_n^{2n-/n-}$, have been obtained. In this approach, a metalloligand such as the tris(oxalato)metallate anion $[M^{III}(C_2O_4)_3]^{3-}$ is used as a ligand in reactions with other metal cations. The templating counterions have an influence on the topology of these compounds. By combining the intrinsic properties of the host, especially the magnetic ones, with additional functionalities derived from the chosen guest molecules, very interesting multifunctional properties can be achieved.[27–32] As these compounds have regular structures and stable frameworks, they generally exhibit good water and chemical durability under the influence of humidity and temperature. In addition, the oxygen atoms of the oxalate group can form complex hydrogen-bonded networks, which are more than suitable for proton conduction. Therefore, 2D and 3D oxalate-bridged frameworks have been extensively studied as proton conductive materials.[33–46]

Due to different compositions, flexibility, electron configurations and valence states, spinel oxides have intrinsic magnetic, optical, electrical and catalytic properties. Therefore, they can be used in many areas of energy storage and conversion, including electrochemical water splitting, metal–air batteries, CO_2 reduction, solid oxide fuel cells and supercapacitors. Generally, in the production of oxide materials, the chosen synthesis process is decisive for the size, dispersity, morphology and crystal structure of the final product, as well as other desired properties.[47–51] Using oxide, carbonate or nitrate precursors, solid-state reactions are used in conventional ceramic processes to produce transition metal oxides; these reactions often require high processing temperatures. Controlling stoichiometry and phase purity in these processes is a challenge.[47,48,52,53] An alternative synthetic route to mixed metal oxides, after reconstructing of the molecular bonding topology and removing the supporting organic groups, is the use of heterometallic coordination compounds as single-source precursors. The excellent stoichiometric control over the metal ratio in the oxide products is made possible by maintaining the elemental composition determined by the molecular precursor during a solid phase transition.[53–57]

In our previous works, in addition to the structural and magnetic properties, we also reported the high room-temperature proton conductivity and the exceptional humidity-sensing properties of heterometallic compounds obtained using an aqueous solution of $[A]_3[Cr(C_2O_4)_3]$ [A = $(CH_3)_2(C_2H_5)NH^+$ or $(CH_3)(C_2H_5)_2NH^+$] as a complex ligand in reaction with other metal ions.[22,46] Motivated by these results, we have expanded investigation of potential proton conducting heterometallic compounds, using the same $[A]_3[Cr(C_2O_4)_3]$ building block in reactions with Mn^{2+} ions and the N-donor ligand 2,2′-bipyridine (bpy). Heterotrinuclear compounds $[NH(CH_3)_2(C_2H_5)]$-$[Mn_2Cr(bpy)_2(H_2O)_2Cl_2(C_2O_4)_3]$ (**1**) and $[NH(CH_3)(C_2H_5)_2]$-$[Mn_2Cr(bpy)_2(H_2O)_2Cl_2(C_2O_4)_3]$ (**2**) were prepared and their structural, magnetic, electrical and precursor properties were investigated.

Considering the thermal decomposition of the metal–organic complexes as a pathway to the oxide materials,[53–64] compounds **1** and **2** were effectively employed in the preparation of Mn_2CrO_4. To the best of our knowledge, this is the first report of the one-step production of the spinel-like Mn_2CrO_4 oxide from heterometallic complexes. In this study, besides the effects of heat treatment on the structural and microstructural properties, the optical and photocatalytic[22,65,66] properties of the material obtained from a molecular precursor were investigated.

Results and discussion

Molecular and crystal structures of compounds 1 and 2

The dark bluish polyhedral crystals of compounds [A][{Mn(bpy)-$(H_2O)Cl(\mu\text{-}C_2O_4)\}_2Cr(C_2O_4)$] [A = $(CH_3)_2(C_2H_5)NH^+$ (**1**) and $(CH_3)(C_2H_5)_2NH^+$ (**2**)] were obtained by slow evaporation of the mixture of aqueous solutions containing the building block $[A]_3[Cr(C_2O_4)_3]$ [A = $(CH_3)_2(C_2H_5)NH^+$ or $(CH_3)(C_2H_5)_2NH^+$] and $MnCl_2{\cdot}4H_2O$ and an ethanolic solution of 2,2′-bipyridine in a molar ratio of 1 : 2 : 2. To include alkylammonium counterions as proton carriers and to synthesise heterometallic systems suitable for proton conductivity research, we used a building block $[Cr(C_2O_4)_3]^{3-}$ containing $(CH_3)_2(C_2H_5)NH^+$ or $(CH_3)(C_2H_5)_2NH^+$ as a counterion.[22,46] The isostructural compounds $[NH(CH_3)_2$-$(C_2H_5)][Mn_2Cr(bpy)_2(H_2O)_2Cl_2(C_2O_4)_3]$ (**1**) and $[NH(CH_3)(C_2H_5)_2]$-$[Mn_2Cr(bpy)_2(H_2O)_2Cl_2(C_2O_4)_3]$ (**2**), crystallizing in the monoclinic space group *C*2/*c*, comprise an alkylammonium cation $(CH_3)_2(C_2H_5)NH^+$ (**1**) or $(CH_3)(C_2H_5)_2NH^+$ (**2**) and the heterotrinuclear oxalate-bridged anion $[Mn(bpy)(H_2O)Cl(\mu\text{-}C_2O_4)Cr$-$(C_2O_4)(\mu\text{-}C_2O_4)Mn(bpy)(H_2O)Cl]^-$ (Fig. 1). The trinuclear anion can be considered to be composed of two $[Mn(bpy)(H_2O)Cl]^+$ units bridged by the $[Cr(C_2O_4)_3]^{3-}$ complex anion, which acts as a bidentate ligand towards each of the manganese atoms (Fig. 1(a)). The chromium atom is located on the twofold axis, and the trinuclear unit has an approximate *C*2 symmetry. In addition, the alkylammonium counterion is disordered over two sites related by the inversion centre, so that each site is exactly half occupied.

According to the Cambridge Structural Database[67] (CSD), compounds **1** and **2** are the first known trinuclear $[Mn^{II}Cr^{III}Mn^{II}]$ compounds with oxalate bridges. A similar bonding topology is found in two copper(II) compounds: $[\{Cu(terpy)(NO_3)$-$(\mu\text{-}C_2O_4)\}_2Cr(C_2O_4)]{\cdot}1.5H_2O{\cdot}CH_3OH$ (terpy = 2,2′:6′,2″-terpyridine) and $[\{Cu(bpy)_2(\mu\text{-}C_2O_4)\}_2Cr(C_2O_4)]NO_3{\cdot}H_2O$.[29,68] Compounds in which Mn^{2+} and Cr^{3+} ions are connected by a bis(bidentate) oxalate bridge and contain alkylammonium cations are usually 2D or 3D coordination polymers.[46,69–72]

The Cr1 atom is bonded to six O atoms arranged in a slightly distorted octahedron. The Cr–O bonds are shorter for terminal O atoms [Cr1–O5 = 1.964(4) Å and 1.969(4) Å for **1** and **2**, respectively] and longer for the bridging oxalate ligands [Cr1–O3 = 1.988(3) for **1** and 1.984(3) Å for **2**, and Cr1–O4 = 1.998(4) Å for **1** and 2.000(4) for **2**]. Coordination of the manganese(II) atom is a distorted octahedron, involving two N atoms from the bpy molecule [Mn–N1 = 2.238(4) Å (**1**) and 2.219(3) Å (**2**) and Mn–N2 = 2.250(5) Å (**1**) and 2.246(4) Å (**2**)], one O atom from the oxalate bridge [Mn1–O2 = 2.194(3) Å and 2.189(4) Å for **1** and **2**, respectively] and the water molecule in the basal plane [Mn–O7 = 2.142(4) Å for **1** and **2**], together with another O atom from the oxalate bridge [Mn1–O1 = 2.324(4) Å and 2.311(4) Å for **1** and **2**, respectively] and the chloride ion in the apical positions [Mn1–Cl1 is 2.4391(15) Å for **1** and 2.4409(14) for **2**]. Selected bond distances for **1** and **2** are listed in Table S1. The distances between chromium(III) and manganese(II) ions through the bis(bidentate) oxalate ligand are 5.5188(10) Å for **1** and 5.5117(10) Å for **2**.

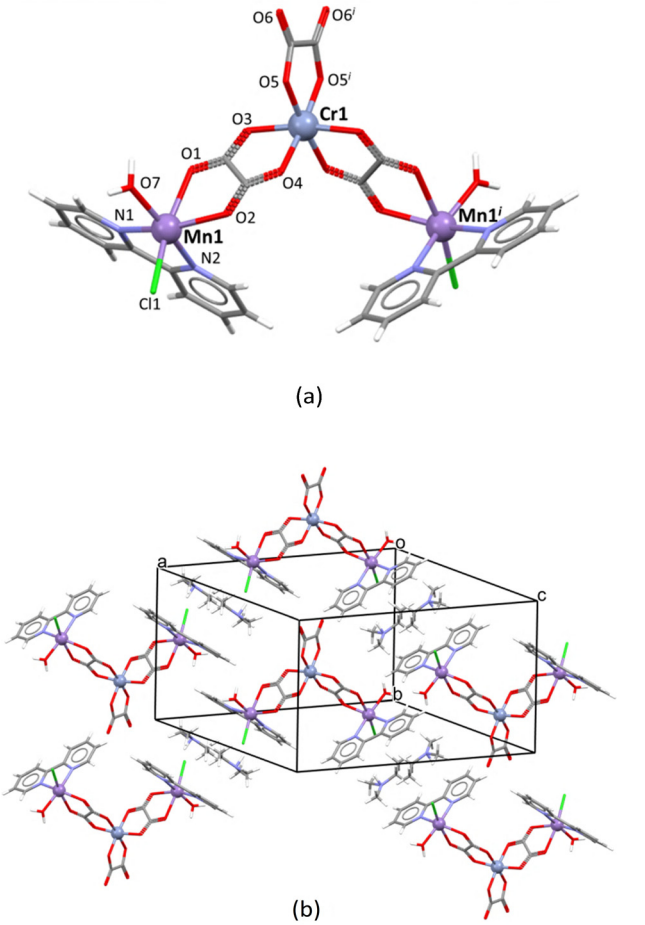

Fig. 1 (a) Heterotrinucler anion $[\{Mn(bpy)(H_2O)Cl(\mu\text{-}C_2O_4)\}_2Cr(C_2O_4)]^-$ in compound **1**, related by the symmetry operator (i) 1 − *x*, *y*, 1/2 − *z*; (b) crystal packing of cations and anions in the (101) plane.

The trinuclear complex units $[\{Mn(bpy)(H_2O)Cl(\mu\text{-}C_2O_4)\}_2$-$Cr(C_2O_4)]^-$ are hydrogen bonded to each other *via* coordinated chloride anions, water molecules and oxygen oxalate atoms, resulting in the supramolecular 2D layers in the (001) plane (Fig. 2 and Fig. S1a). Although both compounds possess only two symmetry-independent hydrogen bonds (O7–H7A···O6 and O7–H7B···Cl1), 2D patterns are formed due to the symmetry properties of the structures. Hydrogen bonding geometry is given in Table S2. As is shown, the oxygen atoms of the terminal oxalate ligand (O6 and $O6^i$; Fig. 1) as hydrogen acceptors are linked to two coordinated water moleules (O7) originating from two $[\{Mn(bpy)(H_2O)Cl(\mu\text{-}C_2O_4)\}_2Cr(C_2O_4)]^-$ units. In addition, two chloride ions (Cl1 and $Cl1^i$) form hydrogen bonds with other hydrogen atoms of water molecules that are coordinated to metal centres of two other neighboring complex anions. Thus, each heterotrinuclear anion forms hydrogen bonds with four neighbouring anions (Fig. S1a). The D···A distances indicate that these hydrogen bonds are relatively strong and arranged around the cavity (Fig. 2 and Table S2). In addition, each trinuclear anion is linked by intermolecular π-stack interactions through the aromatic rings of the 2,2′-bipyridine ligands with neighbouring

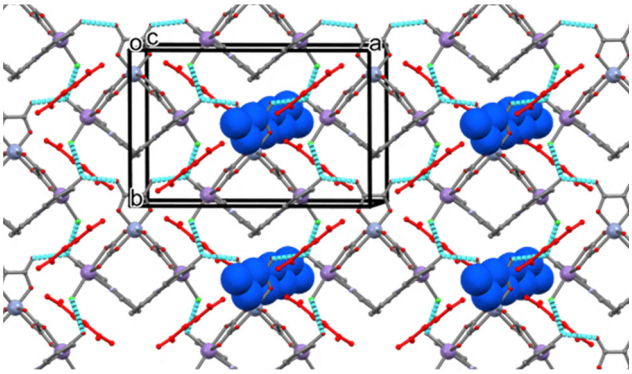

Fig. 2 Crystal packing in the (001) plane achieved thorough hydrogen bonds between anions (cyan sticks) in compound **1**. Disordered cations are depicted in red. The structure contains voids (depicted in blue) running perpendicular to the hydrogen bonding network in the (001) plane.

units forming alternating sandwich-like π-stacks in the [001] direction (Fig. S1b and Table S3).

Infrared study

The FTIR-ATR spectra of the prepared complexes agree with the results of the X-ray analysis: the presence of oxalate groups, an aromatic N-donor ligand and alkyl-substituted ammonium cations can be deduced from the spectra (Fig. S2). The absorption bands corresponding to the stretching vibrations of the bidentate and bis(bidentate) oxalate groups are summarized for both compounds in Table S4. Due to the presence of alkylammonium cations in **1** and **2**, the bands of medium intensity located in the range of 3180–2800 cm^{-1} could be recognized as ν(C–H).[19,26,46] Two overlapping bands appear in the higher frequency part of the FTIR-ATR spectra for both compounds, indicating ν(O–H) and ν(N–H) stretching vibrations originating from the coordinated water molecule and the protonated alkylamine nitrogen, respectively. Both bands, centred at 3520 and 3338 cm^{-1}, are very broad, which is consistent with the hydrogen bonding of the OH and NH groups between the molecules observed in the crystal structure (Table S2).[73] Other bands present in the spectra can be explained by the vibrations of the corresponding bonds of coordinated molecules such as 2,2′-bipyridine.

Thermal study

Thermogravimetric (TG) analysis was used to investigate the thermal stability of the title compounds **1** and **2** on the crystalline samples (Fig. S3) in an oxygen stream up to 800 °C. For both compounds, the character of the thermal decomposition is very similar and the corresponding curves are shown in Fig. S4. The compounds undergo several successive decomposition processes starting at ~120 °C and ending at ~500 °C. The release of the water molecules, the alkylammonium cation, chloride ions, bpy molecules and oxalate groups is responsible for most of the mass loss (exp. 79.76%, calcd 80.65% for **1**; exp. 83.79%, calcd 80.94% for **2**) with some closely and indistinguishable three steps in the TG curve followed by obvious changes in the color and shape of the crystals in hot-stage micrographs. Thereafter, the remaining mass remains constant, with the final black residue corresponding to the spinel oxide, as studied by powder X-ray diffraction (PXRD).

The first mass loss on the TG curves up to 240 °C corresponds to the dehydration process, the loss of two water molecules, and the loss of the alkylammonium cation. After this step, there is a sudden decrease in mass due to the release of the chloride ions and bipyridine molecules. This elimination ends at around 345 °C and partially overlaps with the final process, the decomposition of the oxalate ligands.[74–77]

Proton conductivity

The proton conductivity of compounds **1** and **2** was measured at different temperatures and relative humidities (RH). Loading with guest water molecules acting as medium is a common strategy to improve proton conductivity by tuning the proton concentration and creating proton transport pathways through hydrogen-bonding arrays.[17] Nyquist plots for samples **1** and **2** are shown in Figs. S5 and S6 and the measured resistances are listed in Table S5. The spectra consist of a well-defined high-frequency semicircle corresponding to the conduction process through the bulk and a small spur at low frequencies, related to the blocking of protons on the surface of the metallic electrodes. To obtain DC conductivity values, each spectrum was modelled using a corresponding equivalent electrical circuit consisting of a parallel combination of a resistor and a constant phase element (CPE 1), representing the bulk response, and an additional constant phase element (CPE 2), representing the electrode polarisation. From the model parameters of resistance (R) and electrode geometry, the DC conductivity was calculated (Fig. S7). The samples were found to be extremely sensitive to the humidity conditions at 25 °C, showing an increase in conductivity (σ) from 9.1×10^{-11} S cm^{-1} at 60% RH to 5.6×10^{-5} S cm^{-1} at 93% RH for **1** and from 7.4×10^{-10} S cm^{-1} at 60% RH to 1.8×10^{-6} S cm^{-1} at 93% RH for **2** (Fig. 3). It is evident that an increase in the relative humidity led to an obvious proton conducting switch, with high on/off ratios of approximately 10^6 for **1** and 10^4 for **2**.[1,11] These results confirm that water-mediated proton transport is responsible for the increase in conductivity of these two compounds. The high humidity provides sufficient water molecules to form a certain gradient in proton carriers which influence the proton conducting pathways. It should be noted, however, that at high humidity, the formation of a surface layer of adsorbed water molecules cannot be ruled out. Such a sorbate layer may contribute to the overall proton conductivity.

Fig. 4 shows the Arrhenius temperature dependence of the conductivity for **1** and **2** measured at 60%, 70%, 80% and 90% RH. From the slope of the straight line in the plot of $\ln(\sigma^*T)$ *versus* $1000/T$, it can be seen that the activation energies (E_a) for the conductivity process are 0.72 eV, 0.70 eV, 0.68 eV and 0.47 eV for **1** and 0.66 eV, 0.52 eV, 0.44 eV and 0.38 eV for **2** as a function of relative humidity. At the selected humidity, the conductivity of **1** and **2** increases slightly with temperature, suggesting that the increase in σ is due to the thermal activity of

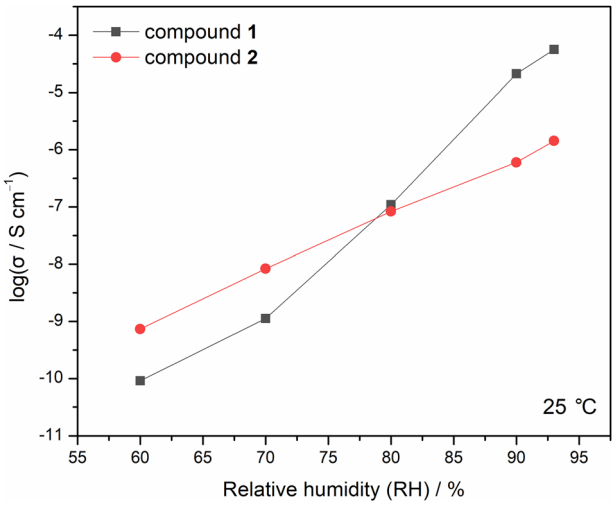

Fig. 3 The proton conductivity as a function of RH at room temperature of compounds $[NH(CH_3)_2(C_2H_5)][Mn_2Cr(bpy)_2(H_2O)_2Cl_2(C_2O_4)_3]$ (**1**) and $[NH(CH_3)(C_2H_5)_2][Mn_2Cr(bpy)_2(H_2O)_2Cl_2(C_2O_4)_3]$ (**2**).

the water molecules, which provides enough energy for the motion, rotation and reorientation of protons, facilitating the transfer of protons as temperature increases (Fig. 4); at 55 °C and 90% RH, the σ values are 9.90×10^{-5} S cm^{-1} for **1** and 2.3×10^{-6} S cm^{-1} for **2** (Table S6).[78] The obtained values of E_a are slightly higher than those typically attributed to a Grotthuss-like proton conduction mechanism in metal–organic frameworks ($E_a < 0.4$ eV), where a proton moves within a hydrogen-bonded network.[13,14] Under low RH conditions, the adsorbed water molecules cannot form effective hydrogen bonds and thus may rather serve as vehicles to carry protons as oxonium ions (vehicle mechanism). As relative humidity increases, the adsorbed water molecules accumulate and begin to form stronger intermolecular bonds that allow proton hopping along the formed hydrogen bonding network within the structures. Accordingly, at high RH, the so-called Grotthuss mechanism dominates the transport process in compounds **1** and **2**. Thus, the proton conduction mechanism changes from the vehicle mechanism to the Grotthuss mechanism with increasing RH. This is another indication that a dense hydrogen bonding network is essential for the high conductivity. Based on the results discussed above, we believe that both the Grotthuss and vehicle mechanisms contribute to the proton conduction process in compounds **1** and **2**.

The chronoamperometry experiment was carried out by applying a voltage of 10 V to a 1 mm thick compact pellet of compound **1** with sputtered gold electrodes on the opposite side of the pellet (diameter 3.5 mm). The RH was changed during the experiment and the current response was measured. Fig. 5 shows two cycles of wetting and drying and thus the reproducibility of these experiments. The sputtered gold electrodes on the surface of the pellet ensured ion blocking, so only electrical current was allowed to pass through the pellet. As the RH increased, the current response also increased, by almost four orders of magnitude. The observed current increase during

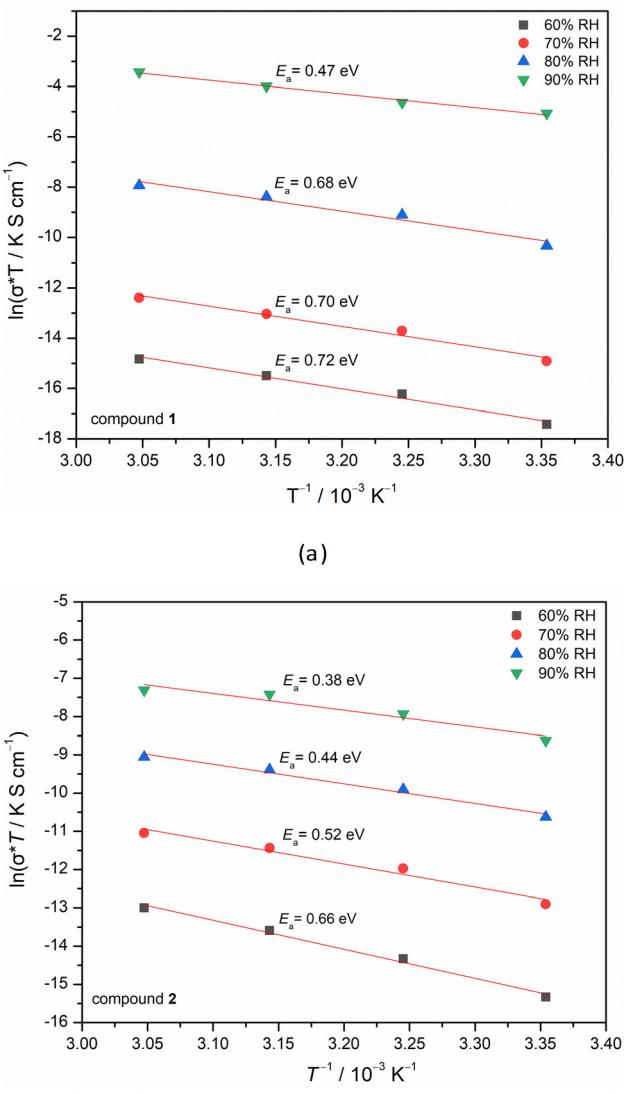

Fig. 4 Arrhenius-type plots of the temperature dependence of the DC conductivity with the corresponding value of activation energy for (a) compound **1** and (b) compound **2**.

wetting and decrease during drying are associated with the diffusion of water molecules and the associated charge exchange,[79] which indicates that the investigated compounds have potential properties as sensing materials. The observed humidity sensing is consistent with investigations of proton conductivity using impedance spectroscopy, which demonstrates how this material creates more conductive routes for protons in wet environments, increasing conductivity overall.

In general, the properties and applications of a material are determined by its structural characteristics. The abilities to adsorb water and to form continuous hydrogen bonding networks are very important factors for proton conduction. Under humid conditions, a suitable chemical potential is created at the grain boundaries and surfaces of the crystals, which causes the incorporation of water molecules into structures with pores

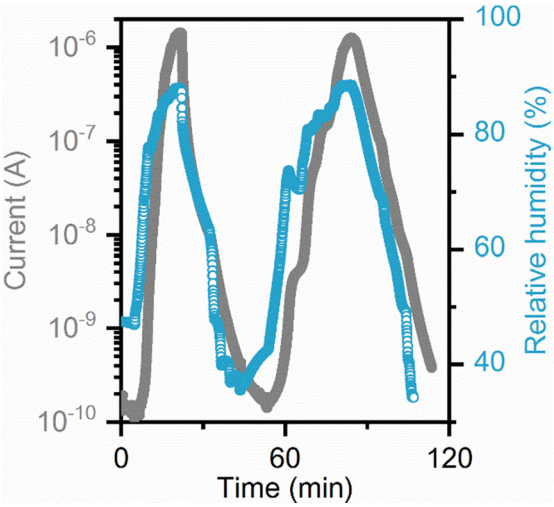

Fig. 5 Chronoamperometric measurements for compound **1** during changes in relative humidity.

and cavities.[79,80] According to void analysis in Mercury,[81] compound **1** contains free space in the crystal structure. The calculated void volume and the position of the void (Fig. 2) are an indication that these structures could accommodate one water molecule per unit cell (the approximate volume for one water molecule is about 40 Å^3).[82] In this way, a long-range-ordered hydrogen bond arrangement can be formed between the proton carriers and the water molecules absorbed in the cavities, which increases the proton conductivity. In addition, in the range of measured humidities, compound **1** has a higher conductivity than compound **2** (Fig. 3). This behaviour is consistent with our previous studies,[22,46] showing that the hydrophilicity of the cationic R_3NH^+ ions generally decreases with increasing bulkiness of the residue, and therefore the $(CH_3)_2(C_2H_5)NH^+$ cation has a higher hydrophilicity compared to the $(CH_3)(C_2H_5)_2NH^+$ cation, leading to a higher affinity for water and consequently a higher proton-conducting property of **1**.

The crystalline nature of coordination compounds allows the structure to be precisely defined, which can lead to a better understanding of the conduction mechanism.[83] In order to explore compounds as promising candidates for the development of advanced materials, their structural integrity must be ensured so that their natural functionalities and properties are preserved under operating conditions. Therefore, stability under wet conditions is always a prerequisite for studying the proton conductivity of coordination compounds.

Photographs of the bulk compounds taken during the acquisition of the FTIR-ATR spectra at 50% and 90% RH (insets in Fig. S2) show that compounds **1** and **2** are stable in a very humid environment. This is also supported by the fact that the position and intensity of the bands in the FTIR-ATR spectra do not change significantly with increasing humidity (Fig. S2). Furthermore, crystals of **1** can be immersed in water without dissolving for a certain period of time (Fig. S8).

In addition to FTIR-ATR, the *in situ* PXRD analysis confirmed that the unit cell parameters (Table 1) of compounds **1** and **2** change slightly under humid conditions (Fig. S9 and S10), supporting the scenario described above. Apart from a small increase in the volume, no changes were observed in the structures after humidity treatment, indicating the stability of compounds **1** and **2**. The difference in the cell volume before and after humidity treatment calculated using the Rietveld refinement corresponds to the volume of a hydrogen bonded water molecule (≈40 Å^3).[82] Since compound **1** has freely accessible cavities, the additional expansion of the unit cell that occurs under humid conditions could lead to the incorporation of a water molecule without significant structural changes. Although a comparable increase in volume occurs for compound **2**, the structure is more compact than in compound **1** and there is no free solvent accessible volume detected in program PLATON.[82]

Table 1 Unit cell parameters of compounds **1** and **2** before and after humidity treatment calculated from the Rietveld refinement

Unit cell parameters	**1**		**2**	
	Dry	Humid	Dry	Humid
a/Å	19.217(4)	19.165(9)	19.235(2)	19.181(0)
b/Å	11.740(1)	11.800(4)	11.732(9)	11.806(9)
c/Å	18.460(9)	18.594(8)	18.439(3)	18.591(4)
β/°	103.8	104.0	103.7	103.9
V/Å^3	4045.59	4080.55	4043.63	4085.32
ΔV/Å^3	35.04		41.69	

Magnetization study

The magnetization M of compounds **1** and **2** is measured as described in the Experimental section and the magnetic susceptibility is calculated from the measurement in the magnetic field H = 1 kOe, whereby this field was chosen due to the linearity of $M(H)$ in the temperature range of 1.8–300 K and to reduce the noise at the same time. The molar susceptibility χ is shown in Fig. 6 as a

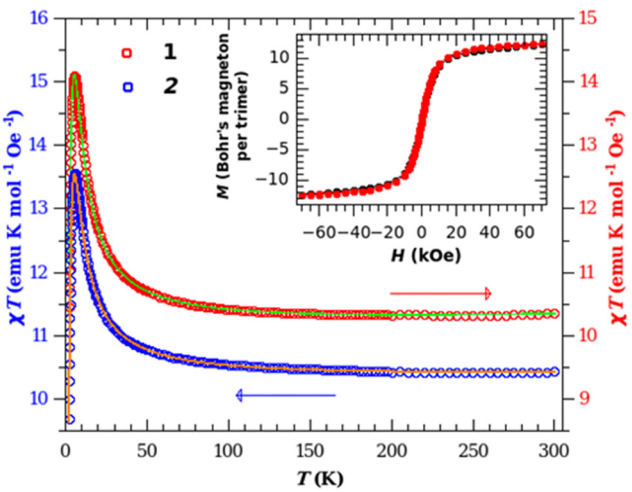

Fig. 6 Temperature dependence of the product between molar susceptibility and the temperature for both compounds. The left and right vertical axes are shifted by 1 unit in order to distinguish the curves. The hollow circles are experimental data and the solid lines are curves of the best fit. The inset shows the isothermal magnetization curves for both compounds.

function of temperature dependence of the product $\chi \cdot T$; in fact, $\chi(T)$ is a less informative visual representation than $\chi \cdot T(T)$ actually is. The temperature dependence of $\chi \cdot T(T)$ in the high temperature range above 200 K becomes nearly constant with the value around 10.4 emu K mol^{-1} Oe^{-1}, which is consistent with the paramagnetic state of two Mn^{2+} ions and one Cr^{3+} ion per formula unit (assuming spins 5/2 and 3/2, respectively, and g-factors of 2.01 and 2.07, respectively). On cooling, the $\chi \cdot T(T)$ starts to increase, with the increase becoming considerable below temperatures of 50 K. This is convincing evidence of ferromagnetic interactions between the spins of the ions, since the zero-field splitting origins cannot cause such large deviations at such relatively high temperatures. In accordance with the crystal structure, the super-exchange can be established between Mn^{2+} and Cr^{3+} ions through oxalate bridges, which are ~5.5 Å apart. Further extension of the interactions to other oxalate-bridged trinuclear [$Mn^{II}Cr^{III}Mn^{II}$] units is not expected due to the considerable distance and the absence of super-exchange bridges. Ferromagnetic interactions are obviously possible between the ions with different spins in the structure shown in Fig. 1.

The modelling of the experimental data is carried out using a self-developed code in the Python programming language. The spin Hamiltonian of the trimer was constructed in a standard form using the spin matrices $\mathbf{S}$ of S = 3/2 for Cr^{3+} and S = 5/2 for Mn^{2+}, with Zeeman terms $-g\mu_B \boldsymbol{H}\cdot\mathbf{S}$ for all three ions and super-exchange terms $-J\mathbf{S}_{Cr}\mathbf{S}_{Mn}$ for both bridges and zero-field splitting $D(\mathbf{S}_z^2 - \mathbf{S}(\mathbf{S}+\mathbf{1})/3)$ for each ion, where J is the super-exchange energy term through both oxalate bridges in a trinuclear unit, D is the zero-field splitting parameter for the corresponding ion, g is the diagonal $\boldsymbol{g}$-tensor with $g_{x,y}$ and g_z components for the corresponding ion, $\boldsymbol{H}$ is the magnetic field vector and μ_B is Bohr's magneton, where the energies J and D are expressed in kelvin. The fitting of the experimental data was performed for both $\chi(T)$ and $\chi \cdot T(T)$. More than 32.000 runs with different initial guesses for the above mentioned fit parameters were completed, performing a full matrix diagonalization and calculation of the magnetization at each measured point. Subsequently, the best fit curves were taken into account for interpretation of the obtained parameters J, D_{Cr}, D_{Mn}, $g_{Cr,z}$, $g_{Cr,xy}$, $g_{Mn,z}$, and $g_{Mn,xy}$. It should be noted that powder averaging is performed on five bands on a sphere, which is a considerably higher order representation than usually used $\chi_z/3 + 2\chi_{xy}/3$. For such demanding calculations, parallel computing on 128 cores was used.

Of all results, the most reliable parameter is the super-exchange interaction J between Mn^{2+} and Cr^{3+} ions bridged by the oxalate ligand. It amounts +1.7 ± 0.1 K (1.18 cm^{-1}), where a positive value indicates a ferromagnetic interaction, and the deviation is determined from 100 best fits. It should be noted that the spins are 5/2 and 3/2. Therefore, it is not surprising that such a relatively small J leads to an observable upturn of $\chi \cdot T(T)$ below 50 K, since the interaction $-J\mathbf{S}_{Cr}\mathbf{S}_{Mn}$ is amplified with large spins. Other parameters are within the usual ranges, namely, g-factors are around 2 and D values are around 0.2 K. Exact details of the $\boldsymbol{g}$-tensors and D values cannot be given due to the over-parametrization and powder approximation, but nevertheless they all agree with the values reported in the literature, where it should be noted that such rigorous fitting converged and reproduced everything consistently without any fixing of parameters. All experimental points are perfectly fitted, and the decrease in the value of the product $\chi \cdot T(T)$ at very low temperatures comes from the zero-field splitting of the metal ions which was taken into account.

An additional confirmation of the ferromagnetic ground state and the ferromagnetic interactions between the ions is the shape of the isothermal $M(H)$ curves measured at 2 K which are shown in the inset of Fig. 6 for both compounds. The magnetization saturates at a value around 13 Bohr's magnetons per trimer formula unit, which is consistent with the feromagnetic coupling of 2 Mn^{2+} and 1 Cr^{3+} unpaired spins. The curve is steeper than the superposition of the curves for three independent spins which points to the ferromagnetic coupling. There is no irreversibility around small fields, confirming the zero-dimensional magnetism of trimers. Moreover, the ZFC-FC curves measured in a small field of 10 Oe showed no bifurcation even at the lowest measured temperatures, which is in accordance with the reversibility of $M(H)$ at 2 K.

As already emphasized, no structurally characterized oxalate-bridged [$Mn^{II}Cr^{III}Mn^{II}$] compound has been found in the literature. The only heterometallic oxalate-bridged dinuclear compound found in CSD,[67] Cat[$MnCr(H_2O)_4(C_2O_4)_3]_2\cdot 6H_2O$ (Cat = bisamidinium cation), indicates ferromagnetic exchange interactions between metal ions mediated by the oxalate bridge (J = +1.6 cm^{-1}).[84] Magnetic measurements of the heterotrinuclear [$Cr^{III}Mn^{II}Cr^{III}$] compound $(TTF)_4[MnCr_2(H_2O)_2(C_2O_4)_6]\cdot 14H_2O$ (TTF = tetrathiafulvalene) show a ferromagnetic coupling (J = 0.54 cm^{-1}), leading to high-spin molecules (S = 11/2). On cooling, the value of the product $\chi \cdot T$ remains almost constant up to 50 K, and below this temperature, it considerably increases with decreasing temperature, indicating the presence of ferromagnetic exchange interactions between the Cr^{3+} and Mn^{2+} ions through the oxalate bridge. The decrease in the value of the product $\chi \cdot T$ at very low temperatures indicates the presence of zero-field splitting of the metal ions.[85,86] A similar behaviour, indicating a weak ferromagnetic interaction between the two terminal Cr^{3+} (S_{Cr} = 3/2) and the central high-spin Mn^{2+} (S_{Mn} = 5/2) ions, is found in compounds containing the same oxalate-bridged anions $(Bpyph)_2[MnCr_2(H_2O)_2(C_2O_4)_6]\cdot 12.5H_2O$ [Bpyph = 1,4-bis(4-pyridyl-1-pyridinio)-phthalazine; J = 0.72 cm^{-1}],[87] $C_4[MnCr_2(H_2O)_2(C_2O_4)_6]\cdot 3H_2O$ (C = 4-aminopyridinium; J = +1.16 cm^{-1}),[88] and $(TDbenz)_2(TsO)_2[Mn(H_2O)_2(C_2O_4)_6]\cdot 6H_2O\cdot 2CH_3OH$ (TDbenz = 1,3,5-tris[2-(1,3-diazolinium)]-benzene; TsO = 4-methylbenzenesulfonate; J = +1.21 cm^{-1}).[89]

Characterization of the Mn_2CrO_4 spinel

Structural and microstructural features. The potential of compounds $[NH(CH_3)_2(C_2H_5)][Mn_2Cr(bpy)_2(H_2O)_2Cl_2(C_2O_4)_3]$ (**1**) and $[NH(CH_3)(C_2H_5)_2][Mn_2Cr(bpy)_2(H_2O)_2Cl_2(C_2O_4)_3]$ (**2**) to act as the single-molecular precursors for the preparation of

spinel oxide Mn_2CrO_4 due to its appropriate composition was explored.[22,58–63]

The normal spinel structure AB_2O_4 generally consists of a closely packed array of O^{2-}, with A^{2+} cations residing on tetrahedral sites and B^{3+} ions on octahedral sites. In regular (normal) spinel structures $^{tet}[A^{II}]^{oct}[B^{III}]_2O_4$, the anions are arranged in close-packed arrays. One eighth of all tetrahedral voids are occupied by divalent A cations, while trivalent B cations are distributed over half of all octahedral sites. It is known that spinels often possess a certain degree of inversion, described by the inversion parameter x. The inversion parameter is defined as the proportion of trivalent B^{3+} cations occupying tetrahedral sites. Some of the main factors that influence the distribution of cations between tetrahedral and octahedral sites are the nature and combination of cations, their radius and charge, the electrostatic contribution of the crystal lattice energy, and the stabilization energy of the crystal field.[90–92] Therefore, the spinel structure can be described by the general formula $^{tet}[A_{1-x}B_x]^{oct}[B_{2-x}A_x]O_4$, considering the inversion parameter x that can take any value between 0 (completely normal spinel structure) and 1 (completely inverse spinel structure). In the completely inverse spinel structure, one eighth of the tetrahedral sites are occupied by (half of the) B^{3+} cations, one quarter of the octahedral sites are occupied by (all of the) A^{2+} cations, and another one quarter of the octahedral sites are occupied by (the other half of the) B^{3+} cations. The exact determination of tetrahedral and octahedral site occupancies becomes even more demanding in the case of Mn-spinel where Mn, as well as other cations of transition metals, can exist in several oxidation states. Apart from reasons connected to the nature of the metal cation, the distribution of cations between tetrahedral and octahedral sites depends significantly on the heat treatment temperature. Although spinels mostly crystallize in the cubic system, there are also cases when, due to the presence of cations that exhibit the Jahn–Teller effect in octahedral coordination, such as the Mn^{3+} cation, tetragonal distortion of the spinel lattice occurs. Such spinels crystallize in the tetragonal space group, $I4_1/amd$.[93–97] The spinel unit lattice in the tetragonal system contains 16 oxygen anions at the Wyckoff position 16*h*. Due to such an arrangement of anions, cations have 16 octahedral (8*d* Wyckoff spot) and 32 tetrahedral (4*a* Wyckoff spot) cavities available.[98]

The comprehensive evolution of the crystalline phase composition as a function of heat treatment during the decomposition of **1** or **2** was conducted using the PXRD measurements on samples previously heated up to 900 °C and then cooled to room temperature (RT) (Fig. 7). Thermal treatment of precursors in the furnace at 500 °C for 3 hours causes the formation of the cubic spinel phase $Mn_{1+x}Cr_{2-x}O_4$ ($0 \leq x \leq 0.7$) and Mn_2O_3 (Fig. S11). In the study by Lu and collaborators,[99] the unit cell parameters for different x values of cubic spinel $Mn_{1+x}Cr_{2-x}O_4$ ($0 \leq x \leq 0.7$) (ranging from 8.4396 Å for $x = 0$ up to 8.4672 Å for $x = 0.7$) are reported.

In this research, unit cell dimension determined by the Rietveld refinement of the pattern obtained after sample treatment at 500 °C (8.4687 Å) matches the unit cell parameter

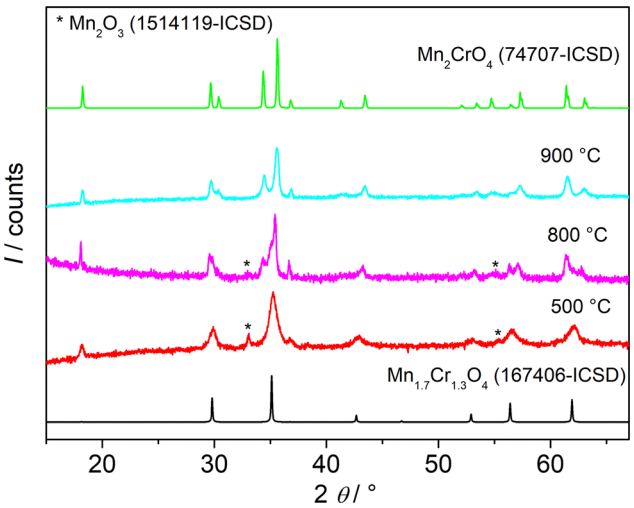

Fig. 7 The PXRD patterns obtained after 3 hour thermal treatment of **2** at 500 °C (red line), 800 °C (magenta line) and 900 °C (aqua line) and cooling to RT. Observable diffraction lines of Mn_2O_3 (1514119-ICSD) are denoted with asterisks. Theoretical diffractograms of spinel $Mn_{1+x}Cr_{2-x}O_4$ ($0 \leq x \leq 1$), where $x = 0.7$ (black line) for $Mn_{1.7}Cr_{1.3}O_4$ (167406-ICSD), and Mn_2CrO_4 (74707-ICSD), where $x = 1$ (green line), are simulated from the database data.

(8.4672 Å) of the model with $x = 0.7$ ($Mn_{1.7}Cr_{1.3}O_4$) (Fig. S11). A further increase in temperature led to a gradual reaction between this spinel and Mn_2O_3 and caused a change in the spinel composition, in which the phase-pure spinel with tetragonal structure Mn_2CrO_4 is formed for $x = 1$ at 900 °C (Fig. 7). This is consistent with the previous results showing that the transition from the cubic to tetragonal phase occurs at $x = 0.8$.[99,100] Such a transition from the cubic to tetragonal structure, also known as macroscopic Jahn–Teller distortion, is related to Mn^{3+} clustering on the octahedral sites in the $Mn_{1+x}Cr_{2-x}O_4$ spinel.[100] The valences of Mn and Cr in stoichiometric $MnCr_2O_4$ are +2 and +3, respectively. While Cr^{3+} ions preferentially occupy octahedral sites, Mn^{2+} ions tend to occupy tetrahedral sites. In tetragonal spinel Mn_2CrO_4, the amount of tetrahedral Mn^{3+} can be disregarded since the Mn^{3+} ions have a large octahedral preferred energy, and its structural formula can be written as $^{tet}[Mn^{II}]^{oct}[Mn^{III}Cr^{III}]O_4$ (Fig. 7 and 8). The Rietveld structure refinement of Mn_2CrO_4 obtained by thermal decomposition of **1** for 3 hours at 900 °C in the furnace and subsequent cooling to RT is shown in Fig. 8; the good agreement of the observed and calculated patterns clearly confirms the formation of the Mn_2CrO_4 phase. The crystal structure is given in the inset of Fig. 8.

It is interesting to note that the literature describing the production and properties of spinel Mn_2CrO_4 is very scarce. It has been found that this oxide can be prepared by the citric acid method using chromium nitrate, manganese acetate and citric acid reagents, as it has been studied as a low-temperature catalyst for the selective reduction to remove NO_x with NH_3.[101] In addition, a series of $Mn_{1+x}Cr_{2-x}O_4$ powders ($x = 0$, 0.1, 0.3, 0.5, 0.7, and 1.0) were synthesized by a sol–gel method from $Mn(NO_3)_2{\cdot}xH_2O$ and $Cr(NO_3)_3{\cdot}yH_2O$.[99] Furthermore, electrical

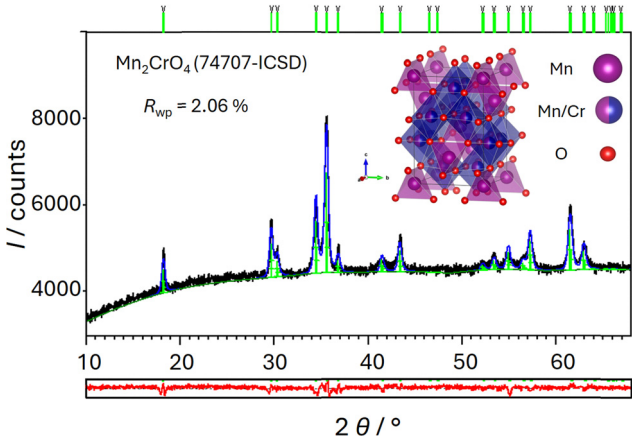

Fig. 8 Observed (solid black line) and calculated (solid blue line) PXRD profiles obtained from the Rietveld refinement against the PXRD data of the Mn_2CrO_4 sample obtained by heating compound **1** at 900 °C for 3 hours followed by cooling to RT. The difference profiles are depicted by the lower solid red line. The green tick marks show the reflection positions of the Mn_2CrO_4 phase (ICSD-74707). The fitted background contribution is shown by the lower solid green line. The inset (top) shows ball and stick representation of $^{tet}[Mn^{II}]^{oct}[Mn^{III}Cr^{III}]O_4$. The Mn_2CrO_4 unit cell is depicted by dashed black lines along the *a* axis.

conduction in $Mn_{1+x}Cr_{2-x}O_4$ spinel occurs *via* a small polaron hopping mechanism.

Surface morphology imaging

The scanning electron microscopy (SEM) images of the Mn_2CrO_4 powder sample prepared by heating metal–organic compound **1** at 900 °C and an annealing time of 3 hours consists of submicron-sized crystals with truncated tetragonal bipyramidal crystal form (see Fig. 9(b)) that are partly sintered and form large sheet-like morphologies (see low magnification Fig. 9(a)). A similar morphology was observed in other spinel oxides (*e.g.* Co_2CrO_4) also prepared using a molecular precursor method.[22] The elemental composition in the bulk oxide samples prepared *via* the molecular precursor route at 600 and 900 °C was investigated by EDX spectroscopy (Table S7 and Fig. S12), revealing that the synthesized material contains Mn, Cr and O elements, which were found in the expected atomic ratios.

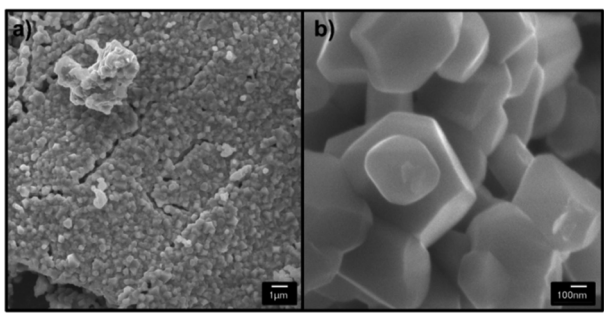

Fig. 9 Low (a) and high (b) magnification SEM images of Mn_2CrO_4 oxide prepared using the molecular precursor route at 900 °C.

UV-Vis spectroscopy measurements and photocatalytic degradation of the MB dye pollutant

The optical properties of the Mn_2CrO_4 phase obtained by heating compound **1** at 900 °C with a holding time of 3 hours were analyzed using UV-Vis diffuse reflectance spectroscopy. As shown in Fig. 10(a), the sample exhibits absorption bands in the visible part of the spectrum measured in the range of 300–1500 nm. Tauc's plot from the diffuse reflectance measurement was constructed to estimate the band gap energy of the prepared oxide. The optical band gap energy of spinel Mn_2CrO_4 oxide was calculated to be 1.4 eV for direct transition (Fig. 10(b)).

The widespread presence of organic dyes in industrial effluents, which are not biodegradable due to their exceptional chemical stability, leads to environmental pollution. The dyes are very harmful and carcinogenic compounds that can affect the quality of groundwater and the natural environment and pose a serious health risk to humans. For these reasons, it is of extreme importance to find a simple and efficient way to treat the wastewater and thus discharge it into the environment. In this context, numerous water treatment methods (physical and biological processes) have already been applied, but they are not sufficient to remove all colorants. Therefore, advanced oxidation processes (AOPs), a class of oxidation techniques in which organic contaminants are degraded to harmless products, have been employed. Thus, the soluble dyes can be removed by photocatalysis by generating *in situ* $OH^{\bullet -}$ radicals that trigger oxidation reactions ending with complete mineralization to CO_2 and H_2O. In this respect, semiconductor photocatalysis is a promising technique for the degradation of organic pollutants.[65,66,102–107]

Many of these oxides are active as photocatalysts under UV light due to their wider band gap (>3 eV). The lowest energy of the band gap suitable for visible light (420 nm < λ < 800 nm) is around 1.55 eV, but there is also growing interest in the use of near-infrared (NIR) light in photocatalysis. To test the photocatalytic activity of the tetragonal spinel oxide Mn_2CrO_4 with an estimated narrow bandgap of ≈1.4 eV, we attempted to

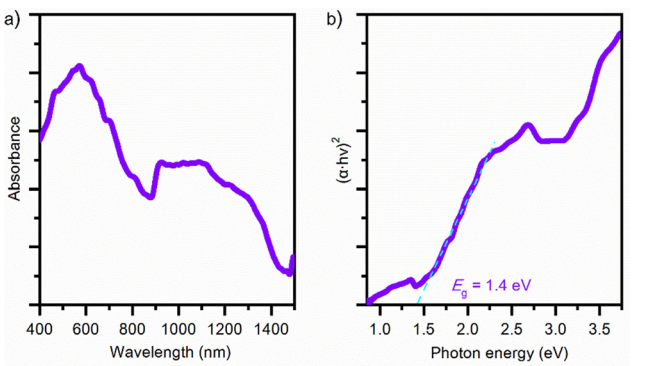

Fig. 10 Optical properties of Mn_2CrO_4 prepared by thermal decomposition of **1** at 900 °C: (a) Kubelka–Munk diffuse reflectance absorption spectrum; (b) Tauc's plot corresponding to direct transition; the dashed red line indicates the band gap energy.

use it for the degradation of organic dye – methylene blue (MB) – under visible light. Photocatalytic materials that can utilize visible light are more attractive than those operating under UV light, and those that work with NIR light are even more interesting since this radiation makes up ≈50% of the solar spectrum.[108–110]

The photocatalytic activity involves the generation of activated electron–hole pairs in the valence band of semiconductors, followed by electron transfer from the valence band to the conduction band in the presence of light energy. The electrons so produced combine with the available oxygen (O_2) molecules in the dye solution to form superoxide anion ($O_2^{\bullet -}$) radicals. On the other hand, the holes in the valence band of Mn_2CrO_4 react with water molecules (H_2O) to produce hydroxyl radicals ($OH^{\bullet -}$). Reactions of the superoxide anions ($O_2^{\bullet -}$) with H_2O produce hydrogen peroxide (H_2O_2) molecules, which decompose into hydroxyl radicals ($OH^{\bullet -}$) in the presence of light. So, these hydroxyl radicals are highly oxidative and break down the organic pollutants into carbon dioxide and water without any byproducts.[111,112]

Any spinel with a narrow band gap, ferromagnetic nature, a high surface area, and low cost should be a good candidate for dye degradation.[65] Fig. S13a displays the optical absorption spectra of the MB dye solutions following various irradiation time intervals in the presence of Mn_2CrO_4 obtained at 900 °C. The blank test was carried out by directly illuminating the dye solutions without a catalyst using a Vis source. The characteristic wavelength, *i.e.* the wavelength at which the absorption coefficient is maximum, is around 663 nm for MB. The intensity of the absorption peak is related to the color concentration of the solution. The degradation efficiency of the MB dye was calculated based on the C/C_0 curves *versus* irradiation time, as shown in Fig. S13c. It can be seen that the degradation efficiency of MB in the presence of the photocatalyst Mn_2CrO_4 was about 14.9%, which represents a very poor photocatalytic performance of the obtained oxide in the degradation of dye under visible light.

To try to enhance the photocatalytic activity of this spinel Mn_2CrO_4 by generating additional highly reactive hydroxyl radicals and by preventing the recombination of holes and electrons, the H_2O_2-assisted degradation was performed. In general, H_2O_2 accepts electrons from the conduction band and immediately converts into $^{\bullet}OH$ radicals, which favors the concentration of holes for the oxidation process. These strongly oxidizing radicals react with the organic dyes and lead to a destructive oxidation process in the dyes.[113,114] Fig. S13b shows that after visible light irradiation, the degradation of the MB dye increases in the presence of H_2O_2, but this catalytic reaction is enhanced to a greater extent when Mn_2CrO_4 is used as a catalyst. About 37.5% of the MB was removed after 180 minutes when H_2O_2 was used, indicating that a small amount of H_2O_2 was activated by visible light. The removal rate reached 54% after 180 minutes when both the catalyst and H_2O_2 were added at the same time under visible light irradiation.

It is difficult to compare the photocatalytic activity of Mn_2CrO_4 obtained *via* the precursor route with the activity of different spinel oxides from the literature, since the performance of photocatalytic systems is highly dependent on various operating parameters that control the photocatalytic degradation of the organic compounds. Some of these factors are the type of photocatalyst, morphology, crystallite size, preparation method, surface area, band gap, porosity, catalyst concentration, pH of the medium, addition of electron acceptors and donors, initial pollutant concentration, irradiation time and light source.[22,65,104,111]

Conclusions

In summary, we report herein the rational design and successful preparation of novel oxalate-bridged heterotrinuclear complexes $[NH(CH_3)_2(C_2H_5)][Mn_2Cr(bpy)_2(H_2O)_2Cl_2(C_2O_4)_3]$ (**1**) and $[NH(CH_3)(C_2H_5)_2][Mn_2Cr(bpy)_2(H_2O)_2Cl_2(C_2O_4)_3]$ (**2**), with the incorporated alkylammonium cation as a proton carrier. By investigating their proton conductivity, we confirmed that low-dimensional oxalate structures, not only 2D and 3D assemblies, can exhibit excellent conductivity behaviour. By introducing guest water molecules as a medium into the cavities of the structures, the proton concentration and the density of the hydrogen bonding arrays are tuned, which has an effect on increasing the conductivity. They show very good sensitivity to stimuli, as a significant increase in proton conductivity is observed with increasing relative humidity, including high on/off ratios of 10^6 for **1** and 10^4 for **2**. As the RH increased, the current response also increased, by almost four orders of magnitude. Compound **1**, which contains a smaller alkylammonium cation, has a higher affinity for water molecules and more voids in the structure and thus a higher proton conductivity. The ferromagnetic coupling between the Cr^{3+} and the high-spin Mn^{2+} ions across the oxalate bridges stabilizes the high-spin ground state (S = 13/2) of the trimeric $[Mn^{II}Cr^{III}Mn^{II}]$ cluster.

The prepared compounds were thoroughly explored as single-source precursors for the formation of the spinel oxide by their thermal decomposition. This molecular precursor-to-material route not only opens a new approach for the production of spinel oxides but also expands the areas of application of coordination compounds. By optimizing the annealing temperature, the phase composition of thermal processing of **1** (or **2**) was evaluated: phase pure spinel Mn_2CrO_4 was obtained by thermal treatment at 900 °C. Unfortunately, the photocatalytic performance was not sufficient to confirm the great potential of the spinel oxide prepared in this way as a photocatalyst for the removal of organic compounds from wastewater in the presence of H_2O_2 under sunlight. An increase in the average particle size reduces the specific surface area, which, in turn, reduces the density of active sites on the surface and also increases the recombination rate of electrons and holes on the surface of the catalysts. Both factors have a negative effect on photocatalytic degradation, which could explain the poor photocatalytic performance of the investigated oxide prepared at 900 °C. On the other hand, the energy band gap decreases

with increasing particle size as the annealing temperature increases.

Experimental section

Materials and physical measurements

All used chemicals were procured from commercial sources and used without further purification. The salt $K_3[Cr(C_2O_4)_3]\cdot 3H_2O$ was prepared using the method described in the literature.[115] The precursor salt $Ag_{0.5}[Ag_{2.5}Cr(C_2O_4)_3]\cdot 3H_2O$ was obtained from the corresponding potassium salt by metathesis.[116] Fourier transform infrared spectra measured in attenuated total reflection mode (FTIR-ATR) were recorded in the 4000–400 cm^{-1} range using a PerkinElmer FT-IR Frontier spectrometer. Thermal properties were investigated from RT to 800 °C in an oxygen stream using a PerkinElmer STA 6000 simultaneous thermal analyzer (a heating rate of 5 °C min^{-1}). The elemental analyses for C, H and N were performed with a PerkinElmer Model 2400 microanalytical analyzer. Scanning electron microscopy (SEM) was performed with a JEOL scanning electron microscope (model JSM-7000 F) operated at 10 keV. An energy-dispersive X-ray (EDX) analyzer integrated with the JEOL SEM was used for elemental analysis of compounds **1** and **2** and the oxides formed at different temperatures.

Synthesis of the precursors $[A]_3[Cr(C_2O_4)_3]$ [A = $(CH_3)_2(C_2H_5)NH^+$ or $(CH_3)(C_2H_5)_2NH^+$]. *N*,*N*-Dimethylethylamine (0.0328 mL; 0.3 mmol) or *N*,*N*-diethylmethylamine (0.0366 mL; 0.3 mmol) was mixed with 37% HCl (0.3 mmol; 1.5 mL) and the reaction mixture was added dropwise to the aqueous solution (3.5 mL) of $Ag_{0.5}[Ag_{2.5}Cr(C_2O_4)_3]\cdot 3H_2O$ (0.0694 g; 0.1 mmol). The reaction mixtures were filtered after the appearance of a white precipitate (AgCl). The remaining dark violet filtrates were used as a precursor for further reactions.

Synthesis of $[A][Mn_2Cr(bpy)_2(H_2O)_2Cl_2(C_2O_4)_3]$ [A = $(CH_3)_2(C_2H_5)NH^+$ (1); A = $(CH_3)(C_2H_5)_2NH^+$ (2)]. Compounds **1** and **2** were synthesized according to the same basic procedure: an aqueous solution of $MnCl_2\cdot 4H_2O$ (0.040 g; 0.200 mmol; 5 mL) and ethanolic solution of the ligand 2,2′-bipyridine (0.031 g; 0.200 mmol; 5 mL) were slowly added to the aqueous solution of the precursor $[NH(CH_3)_2(C_2H_5)]_3[Cr(C_2O_4)_3]$ or $[NH(CH_3)(C_2H_5)_2]_3[Cr(C_2O_4)_3]$ (0.100 mmol; 5 mL). The beaker containing the reaction mixture was allowed to evaporate slowly. During 3 weeks of evaporation to dryness, dark bluish polyhedral crystals of compound **1** or **2** were formed. The crystals were separated mechanically, washed with absolute ethanol and dried in air (≈40% yield). $C_{30}H_{32}Cl_2Mn_2CrN_5O_{14}$ (**1**; Mr = 919.39): calcd. C 39.19, H 3.51, N 7.62%; found C 40.03, H 3.72, N 7.57%. $C_{31}H_{34}Cl_2Mn_2CrN_5O_{14}$ (**2**; Mr = 933.42): calcd C 39.89, H 3.67, N 7.50%; found C 40.01, H 3.89, N 7.35%. The EDX analysis demonstrated a Mn : Cr ratio of 2 : 1 for both compunds (Table S7).

Single-crystal X-ray structural study

The X-ray data for single crystals of compounds **1** and **2** were collected by ω-scans on a Rigaku Oxford Diffraction Synergy S diffractometer using CuKα radiation at 293(2) K (**1**) and 100(2) K (**2**). Data reduction, including the multi-scan absorption correction, was performed using the CrysAlisPRO[117] software package. The structures were solved using SHELXT[118] and refined using SHELXL-2017/1 within the WinGX software package.[119] The full-matrix least squares refinement was used to refine the models; all non-hydrogen atoms were refined anisotropically. The cations in both compounds are disordered about an inversion centre; relatively high residual density points out that an orientational disorder (with two likely orientations) is likely. However, these two positions could not be properly resolved. The C–C and C–N bonds of the cations were restrained to 1.54(4) and 1.47(4) Å, respectively. Hydrogen atoms were constrained to a 'riding model'. Molecular geometry calculations were carried out using PLATON[82] and the figures were obtained using ORTEP[119] and CCDC-Mercury.[81] Crystallographic and refinement data for the structures reported in this study are shown in Table S8.

Thermal synthesis of the Mn_2CrO_4 oxide

Finely ground crystalline powder of **1** (or **2**) was heated in a furnace (Nabertherm, Model LHT 02/16) in a platinum crucible from RT to a certain temperature level, in the range of 400–900 °C, in air with a constant rate of 5 °C min^{-1}, and then cooled down in the same manner to RT. The resulting materials were held at each temperature for 3 hours. After decomposition, the resulting oxide products were characterized by PXRD at RT. Additionally, thermal decomposition of the finely ground crystalline powders of **1** (or **2**) was recorded using a hot-stage microscope (Nikon Aclipse LV150NL hot-stage microscope equipped with a Linkam T95-PE camera) in the temperature range of RT to maximal 600 °C at a heating rate of 10 °C min^{-1} and a stabilization period of 1 hour at each temperature of interest (150, 200, 300, 400, 500 and 600 °C).

Powder X-ray structural study

The structural properties of powder samples **1** and **2**, as well as the resulting oxides after decomposition in the furnace, were investigated at RT by PXRD using a monochromatic Cu Kα X-ray source (λ = 1.54056 Å) on a Malvern Panalytical Empyrean powder diffractometer in the range of 5° to 50° 2θ. The *in situ* PXRD measurements were performed for compounds **1** and **2** when exposed to humid conditions.

Rietveld refinement was performed using an X'Pert HighScore Plus, version 4.1 (PANalytical, 2014), with a pseudo-Voigt function used for describing the profles. A polynomial function was used as the background model. In the course of the Rietveld refinement, the following parameters were refined: scale factor, unit cell parameters, *W*, *V*, shape parameter, asymmetry as well as the atomic coordinates of the oxygen atom.

Electrical study

For the electrical measurements, polycrystalline samples of **1** and **2** (Fig. S3) were prepared in the form of pellets with thicknesses of 1.40 mm (r = 5 mm) and 0.66 mm (r = 14 mm), respectively. The electrical conductivity of the samples was measured using impedance spectroscopy (Novocontrol

Alpha-A high performance frequency analyzer) in a frequency range of 1 Hz to 1 MHz applying a voltage of 0.1 V. Samples were placed between gold-plated electrodes, and two-wire mode was used. Humidity-dependent measurements were carried out by placing the cell inside an Espec SH-242 climate chamber to individually control temperature and humidity. The samples were allowed to equilibrate to the desired humidity (60, 70, 80, and 90% RH) over night and then the temperature was increased (25, 35, 45 and 55 °C) with an equilibration time of 2 hours per step before adjusting the humidity again over night.

Chronoamperometric measurements were performed with a PalmSens4 potentiostat on compressed powder samples.

Magnetization study

Magnetic measurements of the polycrystalline samples of **1** and **2** (Fig. S3) were performed with an MPMS3 SQUID magnetometer. All data were corrected for the contribution of the capsule in which the powder samples were placed. The temperature dependence of the DC magnetization, $M(T)$, was measured in the magnetic fields of 1 kOe and 10 kOe, always after they were stabilized at the measurement temperature, which was between 1.8 and 300 K. In small fields of 10 Oe, the $M(T)$ curves were measured twice: first when the samples were cooled in the zero magnetic field and then measured when heated in the measuring field of 10 Oe (ZFC curve – zero-field cooled), and the second time after they were cooled in this magnetic field (FC curve – field cooled) and also measured when heated. No ZFC-FC splitting was observed and therefore measurements in small fields are not discussed, especially because of the observable noise in the high temperature region. Furthermore, the field dependence of the magnetization was measured at a temperature of 2 K in a full cycle of fields of ±70 kOe in both directions, with no hysteresis observed.

UV-Vis spectroscopy measurements

UV-Vis diffuse reflectance spectroscopy was performed on a Shimadzu UV-Vis-NIR spectrometer (model UV-3600) equipped with an integrating sphere. Barium sulphate was used as a reference. The diffuse reflectance spectra were transformed using the Kubelka–Munk function and the optical bandgaps were estimated from Tauc's plots.[120]

Photocatalytic experiments

The photocatalytic activity of Mn_2CrO_4 was evaluated at RT by the degradation of aqueous solutions of methylene blue (MB) dye under Vis irradiation. 1.0 mg of the powder sample was dispersed in 6.0 mL of a 5 ppm aqueous MB dye solution. Prior to irradiation, the suspension was stirred in the dark for 1 hour to ensure the establishment of adsorption/desorption equilibrium. In the experiment with H_2O_2 assistance, 50 μL of 30% H_2O_2 was added to the above reaction solution and stirred for 30 minutes without exposure to light. Then, 14 Vis lamps (Hg lamp, 8 watt, 400–700 nm) were turned on to start the photodegradation in a photoreactor (Luzchem LZC-4V). A magnetic stirrer was placed at the bottom of the cell to keep the mixture in complete suspension. After irradiation, aliquots with a volume of 3 mL were taken at regular intervals and centrifuged at 9000 rpm for 10 minutes. The photocatalytic degradation reactions were monitored by measuring the concentration of a degraded supernatant liquid as a function of irradiation time by UV-Vis absorption spectra using a UV-Vis spectrophotometer (Varian Cary 60). The concentrations of MB were determined by measuring their absorbance at 663 nm. Blank experiments without photocatalysts were performed prior to the experiments.

Conflicts of interest

There are no conflicts to declare.

Data availability

The data supporting this article are given in the Supplementary information.

Supplementary information: Selected bond distances in **1** and **2** (Table S1), 2D hydrogen-bonding layer and sandwich-like π-stack fragments in **1** (Fig. S1), hydrogen bonding geometry (Table S2), geometric parameters of the aromatic stacking interactions (Table S3), FTIR-ATR spectra (Fig. S2), selected absorption bands in the FTIR-ATR spectra (Table S4), Rietveld refinement for powder samples (Fig. S3), TG curves (Fig. S4), Nyquist plots (Fig. S5 and S6), equivalent circuit model (Fig. S7), microscopy image of crystal agglomerates of **1** (Fig. S8), *in situ* PXRD patterns before and after humidity treatment (Fig. S9 and S10), resistance and proton conductivity values measured at different temperatures and relative humidities (Tables S5 and S6), PXRD data obtained after thermal treatment of **2** at 500 °C (Fig. S11), SEM-EDX microanalysis (Table S7), EDX spectra of Mn_2CrO_4 (Fig. S12), time-dependent UV-Vis absorption spectra of the decomposition of MB (Fig. S13), crystallographic data, and structure refinement details and data collection (Table S8). See DOI: https://doi.org/10.1039/d5tc02569a.

CCDC 2444014 and 2444015 contain the supplementary crystallographic data for this paper.[121a,b]

Acknowledgements

This work was funded and supported by the Croatian Science Foundation under project no. IP-2019-045742. D. P. thanks Dario Barišić, who performed the coding of the fitting program, while the fitting of the experimental data was performed using the Advanced Computing Service provided by the University of Zagreb, the University Computing Centre – SRCE on the Supek and Padobran@Vrančić resources. D. P. acknowledges the support of the project CeNIKS cofinanced by the Croatian Government and the European Union through the European Regional Development Fund – Competitiveness and Cohesion Operational Programme (grant KK.01.1.1.02.0013).

Notes and references

1 F. Xiang, S. Chen, Z. Yuan, L. Li, Z. Fan, Z. Yao, C. Liu, S. Xiang and Z. Zhang, Switched proton conduction in metal–organic frameworks, *J. Am. Chem. Soc. Au*, 2022, **2**, 1043–1053.

2 F. Lang, J. Pang and X.-H. Bu, Stimuli-responsive coordination polymers toward next-generation smart materials and devices, *eScience*, 2024, **4**, 100231.

3 Q. Guan, Y. Fang, X. Wu, R. Ou, X. Zhang, H. Xie, M. Tang and G. Zeng, Stimuli responsive metal organic framework materials towards advanced smart application, *Mater. Today*, 2023, **64**, 138–164.

4 F. Bigdeli, C. T. Lollar, A. Morsali and H.-C. Zhou, Switching in Metal–Organic Frameworks, *Angew. Chem., Int. Ed.*, 2020, **59**, 4652–669.

5 Y. Nagao, Proton-Conducting Polymers: Key to Next-Generation FuelCells, Electrolyzers, Batteries, Actuators, and Sensors, *ChemElectroChem*, 2024, **11**, e20230084.

6 W.-H. Li, W.-H. Deng, G.-E. Wang and G. Xu, Conductive MOFs, *EnergyChem*, 2020, **2**, 100029.

7 P. Ramaswamy, N. E. Wong and G. K. H. Shimizu, MOFs as proton conductors – challenges and opportunities, *Chem. Soc. Rev.*, 2014, **43**, 5913–5932.

8 X. Meng, H.-N. Wang, S.-Y. Song and H.-J. Zhang, Proton-conducting crystalline porous materials, *Chem. Soc. Rev.*, 2017, **46**, 464–480.

9 K. Müller, J. Helfferich, F. Zhao, R. Verma, A. B. Kanj, V. Meded, D. Bléger, W. Wenzel and L. Heinke, Switching the Proton Conduction in Nanoporous, Crystalline Materials by Light, *Adv. Mater.*, 2018, **30**, 1706551.

10 D. Shao, W.-J. Tang, Z. Ruan, X. Yang, L. Shi, X.-Q. Wei, Z. Tian, K. Kumari and S. K. Singh, Water-driven reversible switching of single-ion magnetism and proton conduction in a dysprosium sulfonate, *Inorg. Chem. Front.*, 2022, **9**, 6147–6157.

11 H. K. Lee, Y. Oruganti, J. Lee, S. Han, J. Kim, D. Moon, M. Kim, D.-W. Lim and H. Ri Moon, Moisture-triggered proton conductivity switching in metal–organic frameworks: role of coordinating solvents, *J. Mater. Chem. A*, 2024, **12**, 795–801.

12 D.-W. Lim, M. Sadakiyo and H. Kitagawa, Proton transfer in hydrogen-bonded degenerate systems of water and ammonia in metal–organic frameworks, *Chem. Sci.*, 2019, **10**, 16–33.

13 K.-i Otake and H. Kitagawa, Control of Proton-Conductive Behavior with Nanoenvironment within Metal–Organic Materials, *Small*, 2021, **17**, 2006189.

14 D.-W. Lim and H. Kitagawa, Proton Transport in Metal–Organic Frameworks, *Chem. Rev.*, 2020, **120**, 8416–8467.

15 Y. Ye, L. Gong, S. Xiang, Z. Zhang and B. Chen, Metal–Organic Frameworks as a Versatile Platform for Proton Conductors, *Adv. Mater.*, 2020, **32**, 1907090.

16 D.-W. Lim and H. Kitagawa, Rational strategies for proton conductive metal–organic frameworks, *Chem. Soc. Rev.*, 2021, **50**, 6349–6368.

17 X.-X. Xie, Y.-C. Yang, B.-H. Dou, Z.-F. Li and G. Li, Proton conductive carboxylate-based metal–organic frameworks, *Coord. Chem. Rev.*, 2020, **404**, 213100.

18 S.-D. Zhu, L. Dong, J.-J. Hu, H.-R. Wen, Y.-B. Lu, W.-H. Deng, C.-M. Liu, S.-J. Liu, G. Xu and Z.-H. Fu, A Proton Conductor Showing an Indication of Singleion Magnet Based on a Mononuclear Dy(III) Complex, *J. Mater. Chem. C*, 2021, **9**, 481–488.

19 A. Lozančić, S. Burazer, S. Renka, K. Molčanov, L. Molčanov and M. Jurić, Proton transport in oxalate compounds of iron(III) containing (alkyl)ammonium cations: The influence of the density of hydrogen bonds on conductivity, *CrystEngComm*, 2024, **26**, 1892–1901.

20 S. Pili, P. Rought, D. I. Kolokolov, L. F. Lin, I. Silva, Y. Q. Chen, C. Marsh, I. P. Silverwood, V. G. Sakai, M. Li, J. J. Titman, L. Knight, L. L. Daemen, A. J. Ramirez-Cuesta, C. C. Tang, A. G. Stepanov, S. H. Yang and M. Schroder, Enhancement of Proton Conductivity in Nonporous Metal–Organic Frameworks: The Role of Framework Proton Density and Humidity, *Chem. Mater.*, 2018, **30**, 7593–7602.

21 Y.-B. Lu, X.-L. Lin, J.-H. Ai, Y.-Z. Cai, S.-Q. Li, R. Li, S.-Y. Zhang, Y.-R. Xie and S.-D. Zhu, Proton conductivity studies on two non-porous coordination complexes with different proton densities, *New J. Chem.*, 2022, **46**, 22088–22097.

22 A. Lozančić, S. Burazer, P. Šenjug, S. Renka, K. Molčanov, D. Pajić, L. Androš Dubraja and M. Jurić, Facile one step preparation of Co_2CrO_4 spinel from heterometallic compounds – Structural, magnetic, electrical and photocatalytic studies, *J. Alloys Compd.*, 2024, **986**, 174087.

23 F. Kobayashi, T. Hiramatsu, K. Sueyasu and M. Tadokoro, Proton Conductive Mononuclear Hydrogen-Bonded Cobalt(II) Spin Crossover Complex, *Cryst. Growth Des.*, 2023, **23**, 1633–1640.

24 S.-L. Yang, Y.-Y. Yuan, F. Ren, C.-X. Zhang and Q.-L. Wang, High proton conductivity in a nickel(II) complex and its hybrid membrane, *Dalton Trans.*, 2019, **48**, 2190–2196.

25 T. Yamada, M. Sadakiyo and H. Kitagawa, High Proton Conductivity of One-Dimensional Ferrous Oxalate Dihydrate, *J. Am. Chem. Soc.*, 2009, **131**, 3144–3145.

26 S. Burazer, K. Molčanov, A. Šantić, T. Klaser, E. Wenger, D. Pajić, Z. Jagličić, J. Popović and M. Jurić, Humidity-Sensing Properties of an 1D Antiferromagnetic Oxalate-Bridged Coordination Polymer of Iron(III) and Its Temperature-Induced Structural Flexibility, *Materials*, 2021, **14**, 5543.

27 L. Kanižaj, L. Androš Dubraja, F. Torić, D. Pajić, K. Molčanov, E. Wenger and M. Jurić, Dimensionality controlled by light exposure: 1D versus 3D oxalate-bridged [CuFe] coordination polymers based on an $[Fe(C_2O_4)_3]^{3-}$ metallotecton, *Inorg. Chem. Front.*, 2019, **6**, 3327–3335.

28 L. Kanižaj, D. Barišić, F. Torić, D. Pajić, K. Molčanov, A. Šantić, I. Lončarić and M. Jurić, Structural, Electrical, and Magnetic Versatility of the Oxalate-Based [CuFe] Compounds Containing 2,2′:6′,2″-Terpyridine: Anion Directed Synthesis, *Inorg. Chem.*, 2020, **59**, 18078–18089.

29 L. Molčanov, P. Šenjug, D. Barišić, D. Pajić, K. Molčanov and M. Jurić, Oxalate-based [$Cu^{II}Cr^{III}$] coordination compounds affected by the tridentate ligand, simple anion, and reactant ratio: structural and magnetic features, *Dalton Trans.*, 2022, **51**, 16292–16306.

30 E. Burzurí, M. J. Martínez-Pérez, C. Martí-Gastaldo, M. Evangelisti, S. Mañas-Valero, E. Coronado, J. I. Martínez, J. R. Galan-Mascaros and F. Luis, A quantum spin liquid candidate isolated in a two-dimensional $Co^{II}Rh^{III}$ bimetallic oxalate network, *Chem. Sci.*, 2023, **14**, 3899.

31 T. Mikołaj Muzioł, N. Tereba, R. Podgajny, R. Pełka, D. Czernia, M. Wísniewski, S. Koter and G. Wrzeszcz, Sorption and Magnetic Properties of Oxalato-Based Trimetallic Open Framework Stabilized by Charge-Assisted Hydrogen Bonds, *Int. J. Mol. Sci.*, 2022, **23**, 1556.

32 M. Clemente-León, E. Coronado, C. Martí-Gastaldo and F. M. Romero, Multifunctionality in hybrid magnetic materials based on bimetallic oxalate complexes, *Chem. Soc. Rev.*, 2011, **40**, 473–497.

33 E. Pardo, C. Train, G. Gontard, K. Boubekeur, O. Fabelo, H. Liu, B. Dkhil, F. Lloret, K. Nakagawa, H. Tokoro, S.-I. Ohkoshi and M. Verdaguer, High Proton Conduction in a Chiral Ferromagnetic Metal Organic Quartz-like Framework, *J. Am. Chem. Soc.*, 2011, **133**, 15328–15331.

34 C. Maxim, S. Ferlay, H. Tokoro, S.-I. Ohkoshi and C. Train, Atypical stoichiometry for a 3D bimetallic oxalate-based long-range ordered magnet exhibiting high proton conductivity, *Chem. Commun.*, 2014, **50**, 5629–5632.

35 M. Sadakiyo, H. Ōkawa, A. Shigematsu, M. Ohba, T. Yamada and H. Kitagawa, Promotion of Low-Humidity Proton Conduction by Controlling Hydrophilicity in Layered Metal–Organic Frameworks, *J. Am. Chem. Soc.*, 2012, **134**, 5472–5475.

36 M. Sadakiyo, T. Yamada and H. Kitagawa, Hydroxyl Group Recognition by Hydrogen-Bonding Donor and Acceptor Sites Embedded in a Layered Metal–Organic Framework, *J. Am. Chem. Soc.*, 2011, **133**, 11050–11053.

37 H. Ōkawa, M. Sadakiyo, T. Yamada, M. Maesato, M. Ohba and H. Kitagawa, Proton-Conductive Magnetic Metal–Organic Frameworks, $\{NR_3(CH_2COOH)\}[M_a^{II}M_b^{III}(ox)_3]$: Effect of Carboxyl Residue upon Proton Conduction, *J. Am. Chem. Soc.*, 2013, **135**, 2256–2262.

38 H. Ōkawa, K. Shigematsu, M. Sadakiyo, T. Miyagawa, K. Yoneda, M. Ohba and H. Kitagawa, Oxalate-Bridged Bimetallic Complexes $\{NH(prol)_3\}[MCr(ox)_3]$ (M = Mn^{II}, Fe^{II}, Co^{II}; $NH(prol)_3^+$ = Tri(3-hydroxypropyl)ammonium) Exhibiting Coexistent Ferromagnetism and Proton Conduction, *J. Am. Chem. Soc.*, 2009, **131**, 13516–13522.

39 M. Sadakiyo, T. Yamada and H. Kitagawa, Rational Designs for Highly Proton-Conductive Metal−Organic Frameworks, *J. Am. Chem. Soc.*, 2009, **131**, 9906–9907.

40 M. Sadakiyo, T. Yamada, K. Honda, H. Matsui and H. Kitagawa, Control of Crystalline Proton-Conducting Pathways by Water- Induced Transformations of Hydrogen-Bonding Networks in a Metal−Organic Framework, *J. Am. Chem. Soc.*, 2014, **136**, 7701–7707.

41 M. Sadakiyo, T. Yamada and H. Kitagawa, Proton conductivity control by ion substitution in highly proton-conductive metal–organic framework, *J. Am. Chem. Soc.*, 2014, **136**, 13166–13169.

42 M. Mon, J. Vallejo, J. Pasán, O. Fabelo, C. Train, M. Verdaguer, S. Ohkoshi, H. Tokoro, K. Nakagawa and E. Pardo, A novel oxalate-based three-dimensional coordination polymer showing magnetic ordering and high proton conductivity, *Dalton Trans.*, 2017, **46**, 15130–15137.

43 S. S. Nagarkar, S. M. Unni, A. Sharma, S. Kurungot and S. K. Ghosh, Two-in-one: inherent anhydrous and water-assisted high proton conduction in a 3D metal–organic framework, *Angew. Chem., Int. Ed.*, 2014, **53**, 2638–2642.

44 S. Tominaka, F. Coudert, T. D. Dao, T. Nagao and A. K. Cheetham, Insulator-to-Proton-Conductor Transition in a Dense Metal–Organic Framework, *J. Am. Chem. Soc.*, 2015, **137**, 6428–6431.

45 X. Wang, T. Qin, S.-S. Bao, Y.-C. Zhang, X. Shen, L.-M. Zheng and D. Zhu, Facile synthesis of a water stable 3D Eu-MOF showing high proton conductivity and its application as a sensitive luminescent sensor for Cu^{2+} ions, *J. Mater. Chem. A*, 2016, **4**, 16484–16489.

46 A. Lozančić, S. Renka, D. Barišić, S. Burazer, K. Molčanov, D. Pajićand and M. Jurić, High Proton Conductivity of Magnetically Ordered 2D Oxalate-Bridged [$Mn^{II}Cr^{III}$] Coordination Polymers with Irregular Topology, *Inorg. Chem.*, 2023, **62**, 9418–9428.

47 Q. Zhao, Z. Yan, C. Chen and J. Chen, Spinels: Controlled Preparation, Oxygen Reduction/Evolution Reaction Application, and Beyond, *Chem. Rev.*, 2017, **117**, 10121–10211.

48 Z. Shao, X. Wu, X. Wu, S. Feng and K. Huang, Synthesis and advantages of spinel-type composites, *Mater. Chem. Front.*, 2023, **7**, 5288.

49 S. Deka, Nanostructured mixed transition metal oxide spinels for supercapacitor applications, *Dalton Trans.*, 2023, **52**, 839–856.

50 V. Tsurkan, H.-A. Krug von Nidda, J. Deisenhofer, P. Lunkenheimer and A. Loidl, On the complexity of spinels: Magnetic, electronic, and polar ground states, *Phys. Rep.*, 2021, **926**, 1–86.

51 J. O. Olowoyo and R. J. Kriek, Recent Progress on Bimetallic-Based Spinels as Electrocatalysts for the Oxygen Evolution Reaction, *Small*, 2022, **18**, 2203125.

52 M. S. Chavali and M. P. Nikolova, Metal oxide nanoparticles and their applications in nanotechnology, *SN Appl. Sci.*, 2019, **1**, 607.

53 H. Lu, D. S. Wright and S. D. Pike, The use of mixed-metal single source precursors for the synthesis of complex metal oxides, *Chem. Commun.*, 2020, **56**, 854–871.

54 M. Jurić, J. Popović, A. Šantić, K. Molčanov, N. Brničević and P. Planinić, Single-Step Preparation of the Mixed Ba^{II}–Nb^{V} Oxides from a Heteropolynuclear Oxalate Complex, *Inorg. Chem.*, 2013, **52**, 1832–1842.

55 L. Androš, M. Jurić, J. Popović, A. Šantić, P. Lazić, M. Benčina, M. Valant, N. Brničević and P. Planinić, $Ba_4Ta_2O_9$ Oxide Prepared from an Oxalate-Based Molecular

Precursor—Characterization and Properties, *Inorg. Chem.*, 2013, **52**, 14299–14308.

56 M. Li, J. Liu, T. Liu, M. Zhang and F. Pan, A versatile single molecular precursor for thesynthesis of layered oxide cathode materials for Li-ion batteries, *Chem. Commun.*, 2018, **54**, 1331–1334.

57 M. Li, K. Yang, J. Liu, X. Hu, D. Kong, T. Liu, M. Zhang and F. Pan, A heterobimetallic single-source precursor enabled layered oxide cathode for sodium-ion batteries, *Chem. Commun.*, 2018, **54**, 10714–10717.

58 J. Habjanič, M. Jurić, J. Popović, K. Molčanov and D. Pajić, A 3D oxalate-based network as a precursor for the $CoMn_2O_4$ spinel: synthesis and structural and magnetic studies, *Inorg. Chem.*, 2014, **53**, 9633–9643.

59 L. Androš, M. Jurić, J. Popović, D. Pajić, K. Zadro, K. Molčanov, D. Žilić and P. Planinić, 1D Heterometallic oxalate compounds as precursors for mixed Ca–Cr oxides – synthesis, structures, and magnetic studies, *Eur. J. Inorg. Chem.*, 2014, 5703–5713.

60 M. Jurić, D. Pajić, D. Žilić, B. Rakvin, K. Molčanov and J. Popović, Magnetic order in a novel 3D oxalate-based coordination polymer $\{[Cu(bpy)_3][Mn_2(C_2O_4)_3]\cdot H_2O\}_n$, *Dalton Trans.*, 2015, **44**, 20626–20635.

61 J. Popović, M. Jurić, D. Pajić, M. Vrankić, J. Zavašnik and J. Habjanič, Effect of the cation distribution and microstructure on the magnetic behavior of the $CoMn_2O_4$ Oxide, *Inorg. Chem.*, 2017, **56**, 3983–3989.

62 L. Androš Dubraja, D. Pajić, M. Vrankić, J. Dragović, M. Valant, M. Benčina and M. Jurić, Single-step preparation of rutile-type $CrNbO_4$ and $CrTaO_4$ oxides from oxalate precursors–characterization and properties, *J. Am. Ceram. Soc.*, 2019, **102**, 6697–6704.

63 L. Molčanov, L. Androš Dubraja, M. Vrankić and M. Jurić, A 3D oxalate-bridged $[Cu^{II}Fe^{II}]$ coordination polymer as molecular precursor for $CuFe_2O_4$ spinel—photocatalytic features, *J. Am. Ceram. Soc.*, 2023, **106**, 2997–3008.

64 E. Coronado, C. Martí-Gastaldo, J. R. Galá-Mascarós and M. Cavallini, Polymetallic Oxalate-Based 2D Magnets: Soluble Molecular Precursors for the Nanostructuration of Magnetic Oxides, *J. Am. Chem. Soc.*, 2010, **132**, 5456–5468.

65 P. J. Shah, A. Unnarkat, F. Patel, M. Shah and P. Shah, A comprehensive review on spinel based novel catalysts for visible light assisted dye degradation, *Process Saf. Environ. Prot.*, 2022, **161**, 703–722.

66 A. Krishnan, A. Swarnalal, D. Das, M. Krishnan and V. S. Saji, A review on transition metal oxides based photocatalysts for degradation of synthetic organic pollutants, *J. Environ. Sci.*, 2024, **139**, 389–417.

67 C. R. Groom, I. J. Bruno, M. P. Lightfoot and S. C. Ward, The Cambridge structural database, *Acta Crystallogr.*, 2016, **B72**, 171–179.

68 M. Jurić, P. Planinić, N. Brničević, D. Milić, D. Matković-Čalogović, D. Pajić and K. Zadro, New Heterometallic (Cu^{II} and Cr^{III}) Complexes – First Crystal Structure of an Oxalate–Bridged Ferromagnetically Coupled $[Cu^{II}Cr^{III}Cu^{II}]$ System, *Eur. J. Inorg. Chem.*, 2006, 2701–2710.

69 C. Train, R. Gheorghe, V. Krstic, L.-M. Chamoreau, N. S. Ovanesyan, G. L. J. A. Rikken, M. Gruselle and M. Verdaguer, Strong magneto-chiral dichroism in enantiopure chiral ferromagnets, *Nat. Mater.*, 2008, **7**, 729–734.

70 G. V. Shilov, N. S. Ovanesyan, S. M. Aldoshin, M. Gruselle, C. Train and C. Guyard-Duhayon, Unexpected formation of chiral single crystals of $\{NH(n\text{-}C_3H_7)_3[Mn^{II}Cr^{III}(C_2O_4)_3]\}$, A 2D oxalate-based material, *J. Coord. Chem.*, 2004, **57**, 1165–1171.

71 N. S. Ovanesyan, V. D. Makhaev, S. M. Aldoshin, P. Gredin, K. Boubekeur, C. Train and M. Gruselle, Structure, magnetism and optical properties of achiral and chiral two-dimensional oxalate-bridged anionic networks with symmetric and asymmetric ammonium cations, *Dalton Trans.*, 2005, 3101–3107.

72 R. Pellaux, H. W. Schmalle, R. Huber, P. Fischer, T. Hauss, B. Ouladdiaf and S. Decurtins, Molecular-Based Magnetism in Bimetallic Two-Dimensional Oxalate-Bridged Networks. An X-ray and Neutron Diffraction Study, *Inorg. Chem.*, 1997, **36**, 2301–2308.

73 M. Mesić, M. Dunatov, A. Puškarić, G. Medak, R. Kruk and L. Androš Dubraja, Engineering solid-state structural transformations and reactions in complexes containing a natural alkaloid for specific switchable properties, *Inorg. Chem. Front.*, 2025, DOI: **10.1039/D5QI01084E**.

74 H. R. C. Ouriques, M. F. S. Trindade, M. M. Conceição, S. Prasad, P. F. A. Filho and A. G. Souza, Kinetics of decomposition of alkylammonium salts, *J. Therm. Anal. Calorim.*, 2004, **75**, 569–576.

75 Q. Yang, S. Chen and S. Gao, Two Mn(II) chloride complexes containing guest molecules, *J. Therm. Anal. Calorim.*, 2007, **89**, 567–571.

76 S. Brini, R. Bucci, V. Carunchio and A. D. Magri, Thermoanalytical behaviour of some dicarboxylato-α-diimine-cobalt(III) complexes, *J. Therm. Anal.*, 1990, **36**, 707–720.

77 L. Androš Dubraja, D. Matković-Čalogović and P. Planinić, Crystal disassembly and reassembly of heterometallic Ni^{II}–Ta^{V} oxalate compounds, *CrystEngComm*, 2015, **17**, 2021–2029.

78 X. Liang, S. Wang, S. Zhang, C. Lin, F. Xie, R. Li, F. Zhang, C. Wen, L. Feng and C. Wan, High proton conductivity modulated by active protons in 1D ultra-stable metal–organic coordination polymers: a new insight into the coordination interaction/ability of metal ions, *Inorg. Chem. Front.*, 2023, **10**, 1238–1254.

79 X. Liu, H. Gao, L. Sun and J. Yao, Generic Air-Gen Effect in Nanoporous Materials for Sustainable Energy Harvesting from Air Humidity, *Adv. Mater.*, 2024, **36**, 2300748.

80 M. Dunatov, K. Molčanov, Z. Štefanić, R. Kruk and L. Androš Dubraja, Interfacial Water Molecules as Agents for Phase Change Control and Proton Conductivity Enhancement in the Ammonium Vanadyl Tartrate System, *Inorg. Chem.*, 2024, **63**, 163–172.

81 C. F. Macrae, I. Sovago, S. J. Cottrell, P. T. A. Galek, P. McCabe, E. Pidcock, M. Platings, G. P. Shields, J. S. Stevens, M. Towler and P. A. Wood, Mercury 4.0: from

visualization to analysis, design and prediction, *J. Appl. Crystallogr.*, 2020, **53**, 226–235.

82 A. L. Spek, Single-crystal structure validation with the program. PLATON, *J. Appl. Crystallogr.*, 2003, **36**, 7–13.

83 R.-Y. Li, H.-T. Liu, C.-C. Zhou, Z.-T. Chu, J. Lu, S.-N. Wang, J. Jin and W.-F. Yan, Ligand substitution induced single-crystal-to-single-crystal transformations in two Ni(II) coordination compounds displaying consequential changes in proton conductivity, *Inorg. Chem. Front.*, 2020, **7**, 1880–1891.

84 C. Maxim, S. Ferlay and C. Train, Binuclear heterometallic M(III)–Mn(II) (M = Fe, Cr) oxalate-bridged complexes associated with a bisamidinium dication: a structural and magnetic study, *New J. Chem.*, 2011, **35**, 1254–1259.

85 E. Coronado, J. R. Galán-Mascarós, C. Giménez-Saiz, C. J. Gómez-García, C. Ruiz-Pérez and S. Triki, Hybrid Molecular Materials Formed by Alternating Layers of Bimetallic Oxalate Complexesand Tetrathiafulvalene Molecules: Synthesis, Structure, and Magnetic Properties of $TTF_4\{Mn(H_2O)_2[Cr(ox)_3]_2\}$ 14 H_2O, *Adv. Mater.*, 1996, **8**, 737–740.

86 E. Coronado, J. R. Galán-Mascarós, C. Giménez-Saiz, C. J. Gómez-García and C. Ruiz-Pérez, Hybrid Organic/Inorganic Molecular Materials Formed by Tetrathiafulvalene Radicals and Magnetic Trimeric Clusters of Dimetallic Oxalate-Bridged Complexes: The Series $(TTF)_4\{M^{II}(H_2O)_2[M^{III}(ox)_3]_2\}\cdot nH_2O$ (M^{II} = Mn, Fe, Co, Ni, Cu and Zn; M^{III} = Cr and Fe; ox = $C_2O_4^{2-}$), *Eur. J. Inorg. Chem.*, 2003, 2290–2298.

87 Y.-Q. Sun, J. Zhang and G.-Y. Yang, Molecular self-assemblies of a p-conjugated redox-active bipyridinium cation with magnetic dimetallic oxalate-bridged trimeric clusters, *Dalton Trans.*, 2006, 1685–1690.

88 E. Pardo, C. Train, R. Lescouëzec, K. Boubekeur, E. Ruiz, F. Lloret and M. Verdaguer, Synthesis, crystal structure and magnetic properties of two oxalato-bridged dimetallic trinuclear complexes combined with a polar cation, *Dalton Trans.*, 2010, **39**, 4951–4958.

89 C. Maxim, E. Pardo, M. W. Hosseini, S. Ferlay and C. Train, The odd association of a C3h trisamidinium cation and tosylate anion with a series of linear oxalate-bridged trinuclear heterometallic complexes, *Dalton Trans.*, 2013, **42**, 4704–4713.

90 T. F. W. Barth and E. Posnjak, The spinel structure: An example of variate atom equipoints, *J. Wash. Acad. Sci.*, 1931, **21**, 255–258.

91 E. Posnjak and T. F. Barth, A New Type of Crystal Fine-Structure: Lithium Ferrite ($Li_2O{\cdot}Fe_2O_3$), *Phys. Rev.*, 1931, **38**, 2234–2239.

92 T. F. Barth and E. Posnjak, Spinel structures: with and without variate atom equipoints, *Z. Kristallogr. – Cryst. Mater.*, 1932, **82**, 325–341.

93 R. Englman and B. Halperin, Cooperative Dynamic Jahn-Teller Effect. I. Molecular Field Treatment of Spinels, *Phys. Rev. B*, 1970, **2**, 75–94.

94 Q. Sun, M. Bijelić, A. B. Djurišić, C. Suchomski, X. Liu, M. Xie, A. M. C. Ng, H. K. Li, K. Shih, S. Burazer, Ž. Skoko, I. Djerdj and J. Popović, Graphene-oxide-wrapped $ZnMn_2O_4$ as a high performance lithium-ion battery anod, *Nanotechnol.*, 2017, **28**, 455401.

95 X. Li, Y. Xu and C. Wang, Suppression of Jahn–Teller distortion of spinel $LiMn_2O_4$ cathode, *J. Alloys Compd.*, 2009, **479**, 310–313.

96 A. Kyono, S. A. Gramsch, Y. Nakamoto, M. Sakata, M. Kato, T. Tamura and T. Yamanaka, High-pressure behavior of cuprospinel $CuFe_2O_4$: Influence of the Jahn-Teller effect on the spinel structure, *Am. Mineral.*, 2015, **100**, 1752–1761.

97 A. J. Carrillo, P. Pizarro and J. M. Coronado, Assessing Cr incorporation in Mn_2O_3/Mn_3O_4 redox materials for thermochemical heat storage applications, *J. Energy Storage*, 2021, **33**, 102028.

98 J. Bhattacharya and C. Wolverton, Relative stability of normal *vs.* inverse spinel for 3d transition metal oxides as lithium intercalation cathodes, *Phys. Chem. Chem. Phys.*, 2013, **15**, 6486–6498.

99 Z. Lu, J. Zhu, E. A. Payzant and M. P. Paranthaman, Electrical Conductivity of the Manganese Chromite Spinel Solid Solution, *J. Am. Ceram. Soc.*, 2005, **88**, 1050–1053.

100 P. Holba, M. Nevřiva and E. Pollert, Tetragonal Distortion of Spinel Solid Solution $MnCr_2O_4$–Mn_3O_4, *Mater. Res. Bull.*, 1975, **10**, 853–860.

101 F. Gao, X. Tang, H. Yi, S. Zhao, J. Wang and T. Gu, Improvement of activity, selectivity and $H_2O\&SO_2$-tolerance of micro-mesoporous $CrMn_2O_4$ spinel catalyst for low-temperature NH_3-SCR of Nox, *Appl. Surf. Sci.*, 2019, **466**, 411–424.

102 M. Farooque Lanjwani, M. Tuzen, M. Yar Khuhawar and T. A. Saleh, Trends in photocatalytic degradation of organic dye pollutants using nanoparticles: A review, *Inorg. Chem. Commun.*, 2024, **159**, 111613.

103 A. Elhalil, W. Boumya, A. Machrouhi, R. Elmoubarki, S. Mansouri, M. Sadiq, M. Abdennouri and N. Barka, Synthesis, characterization and effcient photocatalytic properties of spinel materials for dye degradation, *Appl. Surf. Sci. Adv.*, 2023, **13**, 100381.

104 V. S. Kirankumar and S. Sumathi, A review on photodegradation of organic pollutants using spinel oxide, *Mater. Today Chem.*, 2020, **18**, 100355.

105 S. Khan, T. Noor, N. Iqbal and L. Yaqoob, Photocatalytic Dye Degradation from Textile Wastewater: A Review, *ACS Omega*, 2024, **9**, 21751–21767.

106 M. Nasrollahzadeh, M. Sajjadi, S. Iravani and R. S. Varma, Green-synthesized nanocatalysts and nanomaterials for water treatment: Current challenges and future perspectives, *J. Hazard. Mater.*, 2021, **401**, 123401.

107 Z. Z. Vasiljevic, M. P. Dojcinovic, J. D. Vujancevic, I. Jankovic-Castvan, M. Ognjanovic, N. B. Tadic, S. Stojadinovic, G. O. Brankovic and M. V. Nikolic, Photocatalytic degradation of methylene blue under natural sunlight using iron titanate nanoparticles prepared by a modified sol–gel method, *R. Soc. Open Sci.*, 2020, **7**, 200708.

108 A. Kudo and Y. Miseki, Heterogeneous photocatalyst materials for water splitting, *Chem. Soc. Rev.*, 2009, **38**, 253–278.

109 S. Y. Tee, K. Y. Win, W. S. Teo, L.-D. Koh, S. Liu, C. P. Teng and M.-Y. Han, Recent Progress in Energy-Driven Water Splitting, *Adv. Sci.*, 2017, **4**, 1600337.

110 D. Kong, Y. Zheng, M. Kobielusz, Y. Wang, Z. Bai, W. Macyk, X. Wang and J. Tang, Recent advances in visible light-driven water oxidation and reduction in suspension systems, *Mater. Today*, 2018, **21**, 897–924.

111 M. Khatun, P. Mitra and S. Mukherjee, Effect of band gap and particle size on photocatalytic degradation of $NiSnO_3$ nanopowder for some conventional organic dyes, *Hybrid Adv.*, 2023, **4**, 100079.

112 A. Ajmal, I. Majeed, R. N. Malik, H. Idrissc and M. Amtiaz Nadeem, Principles and mechanisms of photocatalytic dye degradation on TiO_2 based photocatalysts: a comparative overview, *RSC Adv.*, 2014, **4**, 37003–37026.

113 M. Waimbo, G. Anduwana, O. Renagi, S. Badhula, K. Michael, J. Park, S. Velusamya and Y. S. Kim, Improved charge separation through H_2O_2 assisted copper tungstate for enhanced photocatalytic efficiency for the degradation of organic dyes under simulated sun light, *J. Photochem. Photobiol. B, Biol.*, 2020, **204**, 111781.

114 K. Tantubay, P. Das and M. Baskey (Sen), Hydrogen peroxide–assisted photocatalytic dye degradation over reduced graphene oxide integrated $ZnCr_2O_4$ nanoparticles, *Environ. Sci. Pollut. Res.*, 2022, **29**, 17309–17318.

115 G. Brauer, in *Handbuch der präparativen anorganischen Chemie*, ed. F. Enke, Stuttgart, Germany, 1981.

116 P. A. W. Dean, D. Craig, I. Dance, V. Russell and M. Scudder, A variable Ag- Cr- oxalate channel lattice: $[M_xAg_{0.5-x}(H_2O)_3]@[Ag_{2.5}Cr(C_2O_4)_3]$, M = K, Cs, Ag, *Inorg. Chem.*, 2004, **43**, 443–449.

117 O. D. Rigaku and P. R. O. CrysAlis, *version: 1.171. 39.46*, Rigaku Oxford Diffraction Ltd, Yarnton, England, 2018.

118 G. M. Sheldrick, SHELXT – Integrated space-group and crystal-structure determination, *Acta Crystallogr., Sect. A: Found. Adv.*, 2015, **71**, 3–8.

119 L. J. Farrugia, WinGX and ORTEP for Windows: an update, *J. Appl. Crystallogr.*, 2012, **45**, 849–854.

120 J. Tauc, R. Grigorovici and A. Vancu, Optical Properties and Electronic Structure of Amorphous Germanium, *Phys. Status Solidi B*, 1996, **15**, 627–637.

121 (*a*) A. Lozančić, S. Burazer, T. Wagner, K. Molčanov, D. Pajić, L. Androš Dubraja, M. Tiemann and M. Jurić, CCDC 2444014: Experimental Crystal Structure Determination, 2025, DOI: **10.5517/ccdc.csd.cc2n1653**; (*b*) A. Lozančić, S. Burazer, T. Wagner, K. Molčanov, D. Pajić, L. Androš Dubraja, M. Tiemann and M. Jurić, CCDC 2444015: Experimental Crystal Structure Determination, 2025, DOI: **10.5517/ccdc.csd.cc2n1664**.